THE ASTROPHYSICAL JOURNAL, 420:213–236, 1994 January 1

ON THE HYDRODYNAMIC INTERACTION OF SHOCK WAVES WITH INTERSTELLAR CLOUDS. I. NONRADIATIVE SHOCKS IN SMALL CLOUDS

RICHARD I. KLEIN[1]
Lawrence Livermore National Laboratory, Livermore, CA 94550; and Department of Astronomy, University of California, Berkeley, CA 94720
CHRISTOPHER F. MCKEE[1]
Departments of Physics and of Astronomy, University of California, Berkeley, CA 94720
AND
PHILIP COLELLA
Department of Mechanical Engineering, University of California, Berkeley, CA 94720
Received 1993 May 28; accepted 1993 July 12

ABSTRACT

The interstellar medium (ISM) is inhomogeneous, with clouds of various temperatures and densities embedded in a tenuous intercloud medium. Shocks propagating through the ISM can ablate or destroy the clouds, at the same time significantly altering the properties of the intercloud medium. This paper presents a comprehensive numerical study of the simplest case of the interaction between a shock wave and a spherical cloud, in which the shock far from the cloud is steady and planar, and in which radiative losses, thermal conduction, magnetic fields, and gravitational forces are all neglected. As a result, the problem is completely specified by two numbers: the Mach number of the shock, M, and the ratio of the density of the cloud to that of the intercloud medium, χ. For strong shocks we show that the dependence on M scales out, so the primary independent parameter is χ. Variations from this simple case are also considered: the potential effect of radiative losses is assessed by calculations in which the ratio of specific heats in the cloud is 1.1 instead of 5/3; the effect of the initial shape of the cloud is studied by using a cylindrical cloud instead of a spherical one; and the role of the initial shock is determined by considering the case of a cloud embedded in a wind.

Local adaptive mesh refinement techniques with a second-order, two-fluid, two-dimensional Godunov hydrodynamic scheme are used to address these problems, allowing heretofore unobtainable numerical resolution. Convergence studies to be described in a subsequent paper demonstrate that ~ 100 zones per cloud radius are needed for accurate results; previous calculations have generally used about a third of this number. The results of the calculations are analyzed in terms of global quantities which provide an overall description of the shocked cloud: the size and shape of the cloud, the mean density, the mean pressure, the mean velocity, the velocity dispersion, and the total circulation.

The principal result of the calculations is that small clouds are destroyed in several cloud crushing times, where the cloud crushing time t_{cc} is the characteristic time for the shock to cross through the cloud. (Quantitatively, $t_{cc} = \chi^{1/2} a_0 / v_b$, where a_0 is the initial cloud radius and v_b is the velocity of the shock in the intercloud medium.) This result, which is consistent with that of Nittman, Falle, & Gaskell (1982) based on calculations at lower resolution, is contrary to the naive expectation that the destruction of the cloud would occur only after it had swept up a column density of intercloud material comparable to that of the initial cloud, which requires a time of order $\chi^{1/2} t_{cc}$. A model in which the Kelvin-Helmholtz instability fragments the cloud into successively smaller pieces is consistent with the numerical results. Contrary to the conclusion of Nittman et al. (1982), cloud material can be accelerated to high velocity by the passage of the shock; a model for the cloud acceleration is developed. A quantitative model for the generation of vorticity in the shock-cloud interaction shows that vorticity is generated at the cloud-intercloud boundary both by the initial passage of the shock and by the subsequent flow of shocked intercloud gas past the cloud. Vorticity is also generated in the intercloud medium when the shock converges on the axis behind the cloud, producing a strong vortex ring which is carried away by the intercloud shock. Swirling motions associated with the vorticity contribute to the destruction of the cloud and produce an observable velocity dispersion perpendicular to the shock of about $0.1 v_b$. A model with a radiative cloud shock ($\gamma_c = 1.1$) is consistent with the recent observations of a possible shocked cloud in the Cygnus Loop supernova remnant (Fesen, Kwitter, & Downes 1992). It is possible that the observed cloud is elongated along the line of sight, however.

Subject headings: hydrodynamics — ISM: clouds — shock waves — supernova remnants

1. INTRODUCTION

The interaction of shock waves with interstellar clouds is a fundamental problem in interstellar gasdynamics. Shock waves are common in the interstellar medium (ISM) because radiative cooling is able to maintain the temperature of most of the gas in the ISM well below the temperatures characteristic of energetic events in the ISM, such as supernovae, stellar winds, bipolar flows, the creation of H II regions, or shocks associated with spiral density waves. A great deal of effort has gone into studying the propagation of shock waves in uniform media, but astrophysical plasmas are generally quite inhomogeneous.

[1] Also Theoretical Astrophysics Center, University of California at Berkeley.

In particular, the ISM is observed to contain both diffuse atomic clouds ($T \sim 10^2$ K, $n \sim 40$ cm^{-3}) and molecular clouds ($T \sim 10$ K, $n \sim 10^3$ cm^{-3}) surrounded by low-density warm gas ($T \sim 10^4$ K, $n \sim 0.3$ cm^{-3}), some of which is photoionized, and a hot coronal gas ($T \sim 10^6$ K, $n \sim 3 \times 10^{-3}$ cm^{-3}).

An understanding of the physics of the interaction of shock waves with interstellar clouds is essential to understanding the evolution of the ISM as it is rent by shock waves from supernovae, stellar winds, cloud-cloud collisions, and spiral density waves (Cox & Smith 1974; McKee & Ostriker 1977). Shock waves produced by supernovae heat the coronal phase of the ISM, determine the velocity dispersion of the clouds, and thereby govern the scale height of the ISM (McKee 1990). Previous calculations (e.g., Nittman, Falle, & Gaskell 1982; Bedogni & Woodward 1990) have suggested that shocks are effective at destroying clouds. Theoretical calculations have indicated that thermal evaporation is also effective at destroying clouds (Cowie & McKee 1977; Nulsen 1982). How then do clouds survive in such a hostile environment? Large volumes of the ISM appear to be filled by hot, low-density gas (Spitzer 1990); how can such coronal gas be preserved if embedded clouds are disrupted by shock waves and dispersed in the hot gas, thereby accelerating the radiative cooling? The hot gas is produced in supernova remnants (SNRs), and it is of some interest to determine how the appearance and evolution of the remnant are affected as the blast wave ablates embedded clouds (Cowie, McKee, & Ostriker 1981; White & Long 1991). Possible examples of the interaction of a blast wave with a cloud have been found in the supernova remnant IC 443 by Braun & Strom (1986) and in the Cygnus Loop by Fesen, Kwitter, & Downes (1992). It has also been suggested that shock compression of interstellar clouds can lead to gravitational instability and the spawning of a new generation of stars (Öpik 1953), but direct observational evidence for this appears to be lacking (Odenwald & Shivanandan 1985).

Interstellar shock waves can be produced by the powerful stellar winds of massive stars as well (e.g., Castor, McCray & Weaver 1975); in this case the clouds may have been altered by photoionizing radiation before the shock strikes the clouds. Young stellar objects of a wide range of masses blow strong winds into their natal molecular clouds (Lada 1985), which are observed to be quite clumpy. Herbig-Haro (HH) objects are shocked regions associated with these outflows. They could represent ambient clouds impacted by the outflow, or high-velocity clouds striking the ambient medium (Schwartz 1983), but in either case they represent examples of the shock-cloud interaction.

We see that the interaction between shocks and interstellar clouds is central to a number of problems in interstellar gasdynamics. More generally, this interaction is a particular example of the interaction between a cloud and a surrounding medium in relative motion. The shock determines the manner in which the cloud is injected into the flow, the accompanying increase in pressure, and the Mach number of the flow past the cloud. A stellar wind bubble provides an example of a variety of flows that can result from a single flow: If a cloud that is struck by the shock driven by a bubble survives the interaction, it will eventually find itself immersed in the hot shocked wind, which has a much smaller Mach number than the shocked ambient medum. In principle, if both the cloud and the bubble survive long enough, the cloud could find itself in the unshocked wind, a very high Mach number flow. We shall see that much of the destructive effect of the cloud-shock interaction is associated with the postshock flow of intercloud gas past the cloud.

Given the importance of the interaction of interstellar shocks with clouds for understanding the structure and the dynamics of the ISM, as well as the possible importance of the interaction as a means of triggering new star formation, the problem has been studied extensively. Analytic discussions have been presented by McKee & Cowie (1975), who focused on the initial stages of the interaction; Spitzer (1982), who demonstrated that slow shocks interacting with clouds would generate substantial amounts of acoustic noise; Heathcote & Brand (1983), who described the overall evolution of the shock-cloud interaction; and McKee et al. (1987), who determined the time evolution of the pressure of a cloud struck by a blast wave. However, in reality the problem represents an extremely complex nonlinear hydrodynamic flow encompassing a rich family of shock-shock interaction phenomena, which means that numerical calculations are required. The first numerical study of this problem was carried out by Sgro (1975), who considered both radiative and nonradiative cloud shocks, and proposed these as models for the quasi-stationary flocculi and the X-ray emission, respectively, in Cas A. His calculation could not resolve the interaction of the shocks in the cloud. A substantial improvement in resolution was made by Woodward (1976) in his pioneering study of the interaction of a spiral density wave shock with an interstellar cloud. He used a combined Eulerian-Lagrangian approach which enabled him to follow the onset of both Rayleigh-Taylor and Kelvin-Helmholtz instabilities, but he could not follow the distortion of the cloud boundary in sufficient detail and stopped the calculation before he could determine the final fate of the shocked cloud. A subsequent investigation of this problem by Nittman et al. (1982) used a flux-corrected transport approach but was very underresolved. As we shall see, however, our calculations bear out their conclusions about the destruction of the cloud. The limiting case of the interaction of a shock wave with a rigid sphere has been discussed by Falle (1989). Krebs & Hillebrandt (1983) considered the problem of inducing gravitational collapse in large clouds that were close to gravitational instability; Oettl, Hillebrandt, & Müller (1985) studied the stabilizing effects of a magnetic field. Tenorio-Tagle & Rozyczka (1986) and Rozyczka & Tenorio-Tagle (1987) used a second-order hydrodynamic scheme to follow the evolution, but again the calculation was underresolved (about 30 zones per cloud radius) and clearly showed the effects of strong numerical diffusion at the interface of the cloud boundary and the intercloud medium; this made it impossible to disentangle the mixing of cloud and intercloud matter due to instabilities from that due to numerical diffusion. Their calculation included realistic radiative cooling in both the cloud and the intercloud gas, but this also served to widen the gap between the resolution needed and that available. They concluded, as had McKee & Cowie (1975) a decade earlier, that shocked clouds do not have the filamentary appearance of observed supernova remnants. Bedogni & Woodward (1990) used a Piecewise-Parabolic Method (PPM; Colella & Woodward 1984) with about 40 zones per cloud radius to achieve somewhat better resolution. They considered six combinations of Mach number M and cloud/intercloud density contrast χ, presenting plots of the evolution of the density and the vorticity in each case. They ignored radiative losses, although this was self-consistent for only two of the cases. Stone & Norman (1992) have reported the first three-dimensional calculations of

the shock-cloud interaction. They found that the vortex rings observed in two-dimensional calculations are unstable. Based on comparison with preliminary results of our two-dimensional calculations (Klein, McKee, & Colella 1990), which extended further in time than their calculation, they confirmed our conclusion that the cloud is completely disrupted by the shock. However, whereas the three-dimensional calculations show a rich structure in the third dimension, Stone & Norman (1992) found that they do not invalidate any of the conclusions drawn from two-dimensional calculations; this result has been verified by Klein, McKee, & Bell (1994b). With the exception of our calculation and that by Woodward (1976), all of these numerical calculations treated the cloud and intercloud media as a single fluid, differing only in density.

Despite the extensive work on this important problem, the key questions remain unresolved: (1) What is the rate of stripping, and what is the total amount of gas stripped from the cloud? What mechanisms are responsible? (2) What is the rate of momentum transfer to the cloud—in other words, how long does it take for the cloud to become comoving with the shocked intercloud medium? (3) What is the appearance of the shocked cloud—its morphology, velocity dispersion, luminosity? (4) How is the interaction between the shock and the cloud affected if the shock in the intercloud medium is itself radiative? (5) Under what conditions will the shocked cloud become gravitationally unstable? (6) How does a magnetic field affect the evolution of the shocked cloud?

In order to address these questions, we have undertaken a comprehensive numerical study of the shock-cloud problem. Preliminary accounts of our results for small, nonradiative clouds have been presented at conferences (Klein et al. 1990; Klein, Colella, & McKee 1992). A parallel study incorporating the effects of the interstellar magnetic field will appear in a subsequent paper (Mac Low et al. 1994). By careful convergence studies (described in Klein, Colella, & McKee 1994a, hereafter Paper II), we have determined that substantially higher resolutions than those used previously—~ 100 zones per cloud radius—are required to represent adequately the complex hydrodynamic processes occurring in this problem. Even higher resolution is required to follow the dynamics when radiative losses are important, since the shock compression can be greater.

In this paper we focus on the simplest case: a steady, planar shock impacting an isolated, spherical cloud under the assumptions that radiation, magnetic fields, gravity, and thermal conduction are all negligible. Since all astrophysical shocks have a finite size and age, the assumption that the shock is steady and planar is equivalent to the assumption that the cloud is sufficiently small compared with the size of the shock. For spherical blast waves, this condition can be quite stringent, limiting the cloud radius to be less than 1% of the radius of the blast wave. This idealization will be relaxed in future work, as will the assumption that radiative losses are negligible. Here it is our intention to establish a benchmark against which these more realistic calculations can be compared. As we shall see, nonradiative shocks always reduce the importance of gravity relative to thermal pressure, so the neglect of gravity remains justified if it is justified initially. The assumption that thermal conduction is negligible is somewhat arbitrary; as we shall see, shocked clouds are thoroughly disrupted, and it is quite possible that the fragments will evaporate.

Because of the simplicity of the problem we consider, it is completely determined by two dimensionless parameters: the Mach number of the shock, M, and the density ratio between the cloud and the intercloud medium, χ. We shall show that the dependence on the Mach number can be scaled out for strong shocks, so the results depend primarily on the density ratio χ. The focus of our calculations is on nonradiative shocks, so that the ratio of specific heats in both the cloud and intercloud medium is 5/3 ($\gamma_c = \gamma_i = 5/3$). However, we shall briefly consider the case $\gamma_c = 1.1$ to get an inkling of the effects of radiative losses from the shocked cloud on the problem.

Our approach to these problems is formulated in § 2. The numerical code and our approach to the analysis of the results are described in § 3. In order to reduce the large quantity of data from the calculations to a manageable form, we have calculated a number of global quantities that characterize the flow, such as the mean velocity, the size and shape of the shocked cloud, and the velocity dispersion. Strong blast waves exhibit a simple scaling as the Mach number of the shock is varied (§ 4). An overall description of the shocked cloud is presented in § 5. Cloud drag is taken up in § 6, in which a simple analytic description is given. Section 7 presents a model for the vorticity generated by the interaction of a shock with a cloud. This vorticity plays a key role in the fragmentation and destruction of the cloud, which is treated in § 8. The interaction of a blast wave with a cylindrical cloud is compared with the standard spherical cloud in § 9; in addition, the interaction of a cloud with a wind is compared with that with a shock in § 9. A brief application of the results to the cloud in the Cygnus Loop observed by Fesen, Kwitter, & Downes (1992) is given in § 10. Finally, § 11 summarizes the results.

2. FORMULATION OF THE PROBLEM

2.1. *Timescales*

Consider a cloud in pressure equilibrium with an ambient medium of density ρ_{i0} (Fig. 1). We shall focus on the case of a spherical cloud with radius a_0, although other cases will be considered as well (see § 9). We assume that the cloud is approximately isothermal; since gravity and magnetic fields have been assumed to be negligible, the cloud will have a nearly uniform density ρ_{c0}. The density contrast between the cloud and the intercloud medium,

$$\chi \equiv \frac{\rho_{c0}}{\rho_{i0}}, \tag{2.1}$$

is expected to be of order 10^2 for cold atomic clouds ($T \sim 10^2$ K) embedded in either the warm neutral medium or the photoionized warm ionized medium ($T \sim 10^4$ K); a similar density contrast is expected for a cloud of warm gas embedded in the coronal gas ($T \sim 10^6$ K). Yet higher density contrasts are possible for molecular clouds ($T \sim 10$ K) embedded in warm gas ($\chi \sim 10^3$) or for cold atomic clouds embedded in coronal gas ($\chi \sim 10^4$). The sound speed is $C = (\gamma P/\rho)^{1/2}$, where P is the pressure. Initially, the sound speed in the cloud is smaller than that in the intercloud medium by a factor $\chi^{1/2}$.

When a shock wave propagating through the intercloud medium at velocity v_b encounters a cloud, it drives a shock into the cloud. The velocity of the cloud shock changes with position in the cloud, but its typical value v_s is given by pressure balance with the shocked intercloud medium. If the shock in the intercloud medium is strong ($M \gg 1$), then the postshock pressure is about $\rho_{i0} v_b^2$. The pressure behind the shock in the cloud is of order $\rho_{c0} v_s^2$. Since these two pressures must be

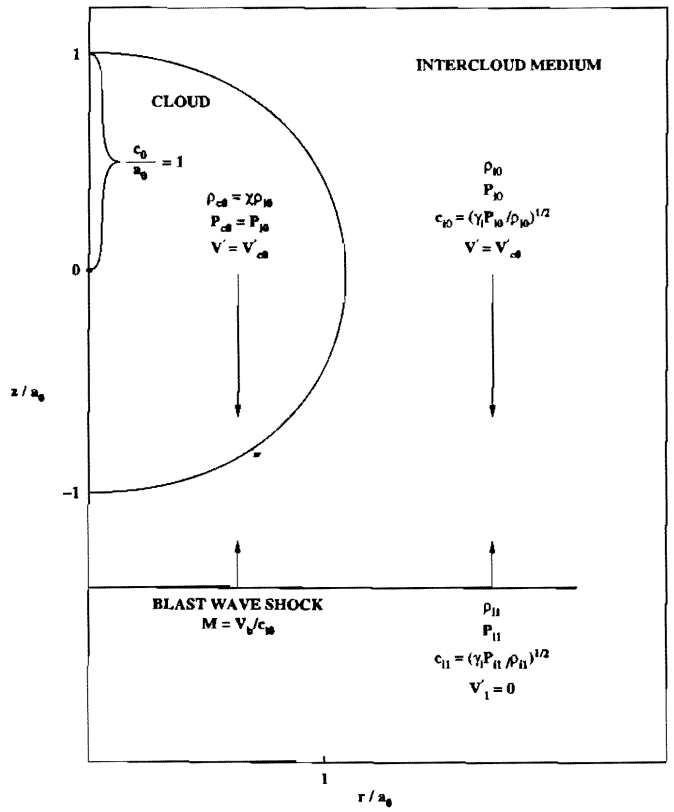

FIG. 1.—Initial conditions for the cloud-shock interaction as viewed in the frame of the shocked intercloud medium. At $t = 0$ the cloud is centered at $z = 0$ and is moving downward at a velocity v'_{c0}. The shock in the intercloud medium (which we term the blast wave shock, although it could be due to a collision between clouds, etc.) is advancing upward at a velocity v'_b. If the shock is strong (Mach number $M \gg 1$), then $v'_b \simeq v_b/4$ and $v'_{c0} \simeq -3v_b/4$, where v_b is the velocity of the blast wave shock as measured in the frame of the unshocked medium (which is usually the frame of the observer). The cloud is assumed to be spherical, with its initial radius in the z-direction, c_0, equal to its initial radius in the radial direction, a_0. The cloud is initially in pressure equilibrium with the intercloud medium, and its density is larger than that in the intercloud medium by a factor χ.

comparable, we conclude that (Bychkov & Pikel'ner 1975; McKee & Cowie 1975)

$$v_s \simeq \left(\frac{\rho_{i0}}{\rho_{c0}}\right)^{1/2}, \quad v_b = \frac{v_b}{\chi^{1/2}}; \tag{2.2}$$

a more accurate expression is given in § 5 below. It is important to note that this result depends on the assumption that the shock in the intercloud medium is nonradiative; the density behind a radiative shock is much greater than ρ_{i0}, and the strength of a cloud shock driven by a radiative intercloud shock would be correspondingly increased.

The time for the shock in the intercloud medium to sweep across the cloud is

$$t_{ic} \equiv \frac{2a_0}{v_b}. \tag{2.3}$$

The characteristic time for the cloud to be crushed by the shocks moving into the cloud is a/v_s. In view of the relation between v_s and v_b given in equation (2.2), we therefore define the *cloud crushing time* to be

$$t_{cc} \equiv \frac{\chi^{1/2}a_0}{v_b}. \tag{2.4}$$

This is the basic timescale governing the evolution of the shocked cloud.

The blast wave accelerates the cloud in two stages (McKee, Cowie, & Ostriker 1978): the cloud shock accelerates it to a velocity v_s, and the flow of shocked intercloud gas then accelerates it until it is comoving with the shocked intercloud gas, which has a velocity $\frac{3}{4}v_b$ (henceforth we adopt $\gamma = 5/3$ for the numerical evaluations in this section). For a large density contrast χ, the cloud shock velocity is small and the acceleration is dominated by the second stage. Let v_c be the mean velocity of the cloud, v_{i1} the velocity of the shocked intercloud medium, and $v'_c = |v_{i1} - v_c|$ the magnitude of the velocity of the cloud relative to the shocked intercloud medium. Then the equation of motion of the cloud can be written

$$m_c \frac{dv'_c}{dt} = -\frac{1}{2} C_D \rho_{i1} v'^2_c A, \tag{2.5}$$

where m_c is the mass of the cloud, $C_D \sim 1$ is the drag coefficient, $\rho_{i1} \simeq 4\rho_{i0}$ is the density of the shocked intercloud medium, and A is the cross-sectional area of the cloud. If A were to remain constant, then equation (2.5) gives the characteristic drag time $t_{drag,0}$ for a strong shock as

$$t_{drag,0} = \frac{\chi a_0}{C_D v_b} = \frac{\chi^{1/2} t_{cc}}{C_D}. \tag{2.6}$$

In fact, the cloud undergoes a lateral expansion after being shocked (Nittman et al. 1982) and the actual drag time t_{drag} is considerably smaller, of the order of a few times the cloud crushing time t_{cc} (§ 6).

After the blast wave has swept over the cloud, the shocked cloud is subject to both the Kelvin-Helmholtz and Rayleigh-Taylor instabilities. For $\chi \gg 1$, the timescale t_{KH} for the growth of the Kelvin-Helmholtz instability for perturbations of wavenumber k parallel to the relative velocity v_{rel} between the cloud and intercloud media is $t_{KH}^{-1} = kv_{rel}/\chi^{1/2}$ (Chandrasekhar 1961). Thus, the Kelvin-Helmholtz growth time is comparable to the cloud crushing time,

$$\frac{t_{KH}}{t_{cc}} = \frac{v_b/v_{rel}}{ka_0}. \tag{2.7}$$

The shortest wavelengths have the fastest growth, but longer wavelengths ($ka_0 \sim 1$) are more disruptive. The deceleration of the shocked cloud initially proceeds on the drag timescale for the initial cloud, $t_{drag,0}$. This gives a deceleration $g \simeq v_b/t_{drag,0} \simeq a_0/t_{cc}^2$, corresponding to a Rayleigh-Taylor growth time given by $t_{RT}^{-1} \simeq (gk)^{1/2}$ (Chandrasekhar 1961). This instability also has a growth time of the order of the cloud crushing time,

$$\frac{t_{RT}}{t_{cc}} \simeq \frac{1}{(ka_0)^{1/2}}. \tag{2.8}$$

These results suggest that the cloud will be destroyed in a time related to the cloud crushing time. Previous simulations (Nittman et al. 1982) and the results presented here show that the cloud destruction time is indeed a few times t_{cc}.

The final timescale of interest is the pressure variation timescale t_P. In many cases, astrophysical shocks are driven by blast waves produced by explosions or winds emanating from a point source, and we can readily estimate t_P for such shocks. Provided that the volume filling factor of the clouds is not

large, such blast waves expand as (Ostriker & McKee 1988)

$$R_b(t) = \left[\frac{\xi E(t)}{\langle \rho_i \rangle}\right]^{1/5} t^{2/5} \propto t^{\eta}, \tag{2.9}$$

where ξ is a constant of order unity, $E(t)$ is the energy of the blast wave at time t, and $\langle \rho_i \rangle$ is the mean density of the intercloud gas in the blast wave. For a point explosion (a Sedov-Taylor blast wave) in a uniform medium ($\langle \rho_i \rangle = \rho_{i0} =$ constant), the exponent η is $\frac{2}{5}$; for a steady wind ($E \propto t$) in such a medium, $\eta = \frac{3}{5}$. If the intercloud mass is dominated by evaporated clouds, η is $\frac{3}{5}$ in the solution developed by McKee & Ostriker (1977) and $\frac{2}{5}$ in the solution of White & Long (1991). If the cloud is located at a distance R_c from the origin of the blast wave, then the age of the blast wave when it strikes the cloud is $t = \eta R_c/v_b$. The pressure behind the blast wave can change on a much shorter timescale, however, because the pressure gradient behind the blast wave shock is often quite steep. For example, McKee et al. (1987) found that the typical pressure variation timescale for a dense cloud in a Sedov-Taylor blast wave is

$$t_P \equiv \left|\frac{\partial \ln P}{\partial t}\right|^{-1} t \simeq 0.2t \simeq 0.1 \frac{R_c}{v_b}, \tag{2.10}$$

where $v_b = dR_b/dt$ is the velocity of the blast wave. The final numerical form also applies to the early, free expansion stage of SNR evolution: the contact discontinuity separating the expanding ejecta from the shocked ISM is at about $0.9R_b$, so for $t \gtrsim t_P$ the cloud will move into the ejecta, thereby changing its pressure substantially. For a stellar wind bubble or for an evaporation-dominated blast wave, the pressure variation is smaller than for a Sedov-Taylor blast wave, and t_P/t is correspondingly greater.

2.2. *Small Clouds*

Comparison of these timescales shows that clouds can be considered to come in one of three sizes, small, medium, or large (McKee 1988). The definitions used here are somewhat different than in the earlier work, however, because we define the sizes with respect to the pressure variation timescale t_P rather than the age t, and the two differ by about a factor of 5 (eq. 2.10). *Small clouds* have $t_{cc} \ll t_P$, so that $a_0 \ll 0.1R_c/\chi^{1/2}$: the cloud is sufficiently small (or, equivalently, the blast wave is sufficiently old and large) that the blast wave does not change significantly as the cloud is crushed and destroyed. [The numerical estimates in this paragraph are for a Sedov-Taylor ($n = \frac{2}{5}$) or freely expanding blast wave, which has $t_P \simeq 0.1R_c/v_b$.] *Medium clouds* satisfy $t_{cc} \gtrsim t_P \gtrsim t_{ic}$, corresponding to cloud radii intermediate between $0.1R_c/\chi^{1/2}$ and $0.05R_c$: the cloud size is such that the blast wave does not change significantly as it sweeps over the cloud, but it does evolve during the time it takes to crush the cloud. If the pressure decreases behind the blast wave shock, the cloud feels an impulsive force from the blast wave. Finally, *large clouds* have $t_{ic} > t_P$, so that $a_0 > 0.05R_c$: the cloud is large enough that the blast wave ages significantly as it sweeps over the cloud, so that the compression on the sides and rear of the cloud is quite different from that for a small or medium cloud.

This paper studies the interaction of shock waves with small clouds. For supernova remnants in either the free-expansion stage or the Sedov-Taylor stage, a cloud with a density contrast of 100 must be smaller than 1% of the radius of the blast wave, a very restrictive condition. For example, the quasi-stationary flocculi in the SNR Cas A have radii $\lesssim 10^{17}$ cm (van den Bergh 1971); the largest ones are thus about 2% of the size of the remnant ("medium" clouds), and only small flocculi count as "small." In any case, since these clouds are visible in emission, the shocks are radiative and therefore beyond the scope of this paper. It has been conjectured that there are lower density clouds in Cas A with nonradiative shocks (Sgro 1975), and our work should apply to them provided that they are sufficiently small. It is clear that much of the nebulosity observed in SNRs does not satisfy the smallness criterion demanded by our idealized calculation and will have to be the subject of future work.

2.3. *Limitations*

2.3.1. *Radiative Cooling*

Radiative cooling is assumed to be negligible, both in the intercloud medium and in the shocked cloud. For a gas of cosmic abundances the cooling rate for temperatures in the range 10^5–$10^{7.5}$ K can be approximated as $n^2\Lambda = 1.6 \times 10^{-19} T^{-1/2} n^2$ in units of ergs cm^{-3} s^{-1} based on the results of Raymond, Cox, & Smith (1976), where n is the hydrogen density. Inserting a factor β_Λ to allow for deviations from this expression, we find that the cooling time behind a strong shock is

$$t_{\rm cool} = \frac{2.3nk_{\rm B}T}{n^2\Lambda} = \frac{2.54 \times 10^{10}}{\beta_\Lambda}\left(\frac{v_{s7}^3}{n_0}\right) \text{s}, \tag{2.11}$$

where $v_{s7} \equiv v_s/(10^7 \text{ cm s}^{-1})$, n_0 is the density ahead of the shock, and the shocked gas has been assumed to be fully ionized, with 2.3 particles per hydrogen atom. This expression should be approximately valid for shock velocities in the interval $1 \lesssim v_{s7} \lesssim 20$. Numerical calculations of the structure of interstellar shocks in the velocity range $0.6 \lesssim v_{s7} \lesssim 1.5$ show that the time for the postshock gas to cool to 10^4 K is within a factor of 2 of the estimate in equation (2.11) with $\beta_\Lambda = 0.77$ (McKee et al. 1987). For timescales much less than $t_{\rm cool}$, radiative cooling has a negligible effect on the dynamics; nonetheless, the amount of radiation emitted may be quite enough to observe.

To ensure that the cloud shock is nonradiative, we require the cooling time behind the cloud shock to exceed the cloud crushing time by a factor of 10 (our longest simulation is almost 10 cloud crushing times). The shock velocity must then satisfy

$$v_{s7} > 3.33(n_{c0}\, a_{\rm pc})^{1/4}, \tag{2.12}$$

where $a_{\rm pc} \equiv a_0/(1 \text{ pc})$. The corresponding postshock temperature (assuming equipartition between electrons and ions) is $1.5 \times 10^6 (n_{c0}\, a_{\rm pc})^{1/2}$ K. (In fact, because the cloud is subject to multiple shocks, this temperature is reached for v_s somewhat less than the value in eq. [2.12]; see § 5.) The lower limit on the blast wave velocity v_b for a nonradiative cloud shock is larger than the value of v_s in equation (2.12) by a factor of $\chi^{1/2}$; for $\chi \gtrsim 10$, this corresponds to $v_b \gtrsim 10^3 (n_{c0}\, a_{\rm pc})^{1/4}$ km s^{-1}.

2.3.2. *Thermal Conduction*

Thermal conduction smooths of out the steep temperature gradients between the shocked intercloud medium and the shocked cloud, and can in principle have a significant effect on the emitted spectrum. The heat flux from the hot intercloud medium into the cloud can lead to evaporation of the cloud. In the absence of a magnetic field, the effects of thermal conduc-

tion on the cloud are determined by the saturation parameter

$$\sigma_0' \equiv \frac{2}{25}\frac{\kappa_i T_i}{\rho_i (C_i/\gamma_i^{1/2})^3 a_0} = 1.67\frac{\lambda_{ee}}{a_0} = 0.39\frac{T_{i7}^2}{n_i a_{pc}} \quad (2.13)$$

(Cowie & McKee 1977; Balbus & McKee 1982), where $\kappa_i = 5.6 \times 10^{-7} T_i^{5/2}$ ergs s^{-1} K^{-1} cm^{-1} is the classical thermal conductivity for a cosmic plasma (Draine & Giuliani 1984), $C_i/\gamma_i^{1/2} = (P_i/\rho_i)^{1/2}$ is the isothermal sound speed, and λ_{ee} is the mean free path for electron-electron energy exchange. For $\sigma_0' \lesssim 0.03$ radiative losses are important, and the hot intercloud gas condenses onto the cloud; for $1 \gtrsim \sigma_0' \gtrsim 0.03$ the classical thermal conductivity is valid and the cloud evaporates; and for $\sigma_0' \gtrsim 1$ the temperature gradient is so steep that T varies over a length scale of several mean free paths and the heat flux saturates. Interestingly, the ratio

$$\frac{\sigma_0'}{t_{cool}/t_{cc}} = 2 \times 10^{-4}\chi^3 \quad (2.14)$$

in the shocked intercloud medium depends only on the density contrast χ. We have assumed that radiative losses in the shocked cloud are negligible ($t_{cool} \gtrsim 10 t_{cc}$), which implies that the heat flux is saturated ($\sigma_0' \gtrsim 1$) if the density contrast exceeds 10.

The rate at which the cloud evaporates can be written in general as

$$\dot{m}_c = 4A\rho_i (C_i/\gamma_i^{1/2}) F(\sigma_0') \quad (2.15)$$

where $F(\sigma_0')$ is a dimensionless quantity of order unity (Cowie & McKee 1977); note that the $F(\sigma_0')$ used here is smaller than that used by Cowie & McKee by the flux-limit parameter $\phi_s \sim 0.3$ (McKee 1988). If we define an ablation time $t_{ab} \equiv m_c/\dot{m}_c$, then behind the blast wave shock we have $\rho_i = 4\rho_{i0}$, $C_i^2 = 5v_b^2/16$, and

$$\frac{t_{ab}}{t_{cc}} = \frac{\chi^{1/2}}{3^{3/2} F(\sigma_0')} \quad (2.16)$$

(McKee 1988). Since $F(\sigma_0')$ is typically of order unity for saturated evaporation, this result shows that typical clouds with $\chi \sim 10^2$ will be ablated by evaporation in a time comparable to the cloud crushing time.

Because we are neglecting thermal conduction we must assume that magnetic fields, too weak to be dynamically significant, strongly inhibit thermal conduction. The result that the factor $F(\sigma_0')$ entering equation (2.16) is of order unity is based on the assumption that heat can be drawn from an approximately spherical volume that is large compared with the cloud. Although this may be valid for a stationary magnetized medium, the flow of the intercloud gas past the cloud will draw the field into a more linear configuration. Balbus (1986) has shown that the evaporation rate is substantially reduced in that case.

2.3.3. *Gravity*

The maximum mass that an unmagnetized, isothermal cloud can have without collapsing under the influence of gravity is (Bonnor 1956; Ebert 1955)

$$m_J = 1.18\left(\frac{P_s^3}{G^3\rho_s^4}\right)^{1/2} \propto \rho_s^{1/2}\left(\frac{P_s}{\rho_s^{5/3}}\right)^{3/2}, \quad (2.17)$$

where G is the gravitational constant and the subscript s denotes quantities evaluated at the surface of the cloud. Observe that m_J is proportional to $(P_s/\rho_s^{5/3})$, which increases with the entropy, and to the square root of the density. Since a shock is an irreversible compression, we conclude that the maximum stable mass increases as a result of a nonradiative shock—in fact, it increases as M^3: self-gravity is unimportant in a cloud struck by a strong shock.

3. NUMERICAL SIMULATIONS

The code we have used will be described in some detail in Paper II, along with a summary of the tests that have been applied to verify its accuracy. It is a two-dimensional code based on local adaptive mesh refinement (AMR) with a Godunov hydrodynamic scheme (Berger & Oliger 1984; Berger & Colella 1989). A rectangular grid is constructed that covers the computational volume (the level 1 grid). The AMR then uses a nested sequence of rectangular meshes to solve the partial differential equations. In practice we have used three levels of grids, with a factor of 4 refinement in each direction; thus, a level 1 grid cell encompasses 256 level 3 cells. The decision to move to a higher level of refinement at any spatial location of the computational domain is based on using Richardson extrapolation to estimate the local truncation error. In addition to setting the refinement level by spatial error estimation, we can directly control the maximum refinement level of cells. We have chosen to allow all cells containing cloud material to be refined to level 3, whereas intercloud material not near the cloud is restricted to lower levels of refinement. The code is a two-fluid code in which the interface between the cloud and intercloud fluids is carefully maintained throughout the calculation. A no-slip boundary condition is applied at the interface. The AMR is applied to both fluids.

We consider a plane shock propagating along the z-axis at velocity v_b (Fig. 1). The cloud is centered on the z-axis, so that the problem is amenable to solution with two-dimensional axisymmetric code. The calculation is carried out in the frame of the shocked intercloud gas, in which the cloud will eventually come to rest. We denote velocities in this frame by a prime; velocities measured in the frame of the unshocked gas, which is often the observer's frame, are unprimed. In the frame of the shocked intercloud gas, the shock propagates in the positive z-direction at a velocity (Landau & Lifshitz 1959)

$$v_b' = \frac{1}{\gamma_i + 1}\left(\gamma_i - 1 + \frac{2}{M^2}\right)v_b \rightarrow \left(\frac{1}{4} + \frac{3}{4M^2}\right)v_b, \quad (3.1)$$

where the numerical evaluation is for $\gamma_i = 5/3$. Initially, the cloud moves downward in the $-z$-direction at a velocity

$$v_{c0}' = -v_{i1} = -\frac{2}{\gamma_i + 1}\left(1 - \frac{1}{M^2}\right)v_b \rightarrow -\frac{3}{4}\left(1 - \frac{1}{M^2}\right)v_b, \quad (3.2)$$

where v_{i1} is the velocity of the intercloud medium just behind the shock as measured in the frame of the unshocked gas.

The resolution of the calculation is specified by the number of level 3 grid spaces that fit in the original cloud radius, a_0. In Paper II we shall demonstrate that accurate results are provided by R_{120}, corresponding to 120 level 3 grids, or 7.5 level 1 grids, in a cloud radius. The computational volume is $16a_0$ in length and $3a_0$ in radius. The shock runs through this volume in a time $16t_{cc}/\chi^{1/2}$. In a number of cases we have extended the calculation beyond this point: at late times, the conditions at the blast wave shock have little effect on the evolution of the shocked cloud.

TABLE 1

CLOUD-SHOCK SIMULATIONS

$\chi = \rho_{c0}/\rho_{i0}$	$M = v_b/C_{i0}$	Resolution[a]
	$\gamma_c = 5/3$	
3.....	10	R_{120}
	100	R_{60}
10.....	10	R_{30}, R_{60}, R_{120}, R_{240}
	100	R_{60}, R_{120}
	1000	R_{120}
30.....	10	R_{120}
	100	R_{60}
100.....	10	R_{120}
	100	R_{60}, R_{120}
	1000	R_{60}
400.....	100	R_{60}
	$\gamma_c = 1.1$	
10.....	10	R_{60}, R_{120}
	100	R_{60}, R_{120}
100.....	100	R_{60}, R_{120}

[a] R_n means a grid resolution of n zones per cloud radius at the third level of refinement.

The problems we have run are summarized in Table 1, which lists the cloud/intercloud density ratio χ; the Mach number of the shock, M; the specific heat ratio in the cloud, γ_c (the intercloud medium always has $\gamma_i = 5/3$); the cloud geometry; and the resolution. Density ratios over the range 3–400 have been considered; the simulations become increasingly time-consuming as the ratio is increased because of the increasing disparity between the Courant time for the cloud and intercloud medium. Cases with Mach numbers of 10, 100, and 1000 were run in order to demonstrate Mach scaling (§ 4). Most of the runs had $\gamma_c = 5/3$, but we also considered the case $\gamma_c = 1.1$ to give an approximation for the effects of radiative losses from the shocked cloud. The cloud was usually assumed to be spherical, but a cylindrical case was considered as well. In addition, we made one run in which the cloud was immersed in a flow that did not have a shock, simulating a cloud immersed in a wind.

The results for a representative sample of the cases we have run are summarized in Tables 2–4. Most of the cases were run for about four cloud crushing times, by which point the cloud has undergone substantial deceleration and destruction. For the "standard case" ($M = \chi = 10$, $\gamma_c = 5/3$) the computation was extended to $9.66t_{cc}$. The tables list the ratio of the analytically estimated sound speed in the shocked cloud to the blast wave velocity,

$$\frac{C_c}{v_b} \simeq \frac{C_c}{\chi^{1/2} v_s} = \left[\frac{2\gamma_c(\gamma_c - 1)}{\chi(\gamma_c + 1)^2}\right]^{1/2} = \begin{cases} 0.56\chi^{-1/2}, & \gamma_c = 5/3, \\ 0.22\chi^{-1/2}, & \gamma_c = 1.1, \end{cases} \tag{3.3}$$

where the estimate is based on the assumption that the cloud is shocked by a single strong shock of velocity $v_b/\chi^{1/2}$. The cloud drag time t_{drag} is the time at which the difference between the cloud velocity and that of the shocked intercloud medium has been reduced by a factor $e = 2.718$. The cloud destruction time t_{dest} is the time at which the mass of the cloud fragment on the axis has been reduced by a factor e. The mixing time t_{mix} provides another estimate of the time it takes to destroy the cloud; it is defined in § 8 below. After an initial compression, the cloud undergoes a lateral expansion until a time t_m; we have estimated t_m from the numerical results as the time at which the cylindrical radius first reaches a value within 10% of its maximum value.

Each two-dimensional hydrodynamic calculation produces a three-dimensional data cube with an enormous amount of information. To compress this information into a manageable form, we define a number of "global quantities" which integrate over the structure of the cloud (see Paper II for a more detailed discussion). The tables contain several of these global quantities evaluated at $t \simeq t_m$. The effective cylindrical and axial radii, a and c, are defined in terms of the rms radial and axial coordinates as follows: Let

$$\langle r^2 \rangle = \frac{1}{m_c} \int \rho_c r^2 \, dV , \tag{3.4}$$

$$\langle z \rangle = \frac{1}{m_c} \int \rho_c z \, dV , \tag{3.5}$$

$$\langle z^2 \rangle = \frac{1}{m_c} \int \rho_c z^2 \, dV . \tag{3.6}$$

Then we define the effective radius normal to the axis of symmetry as

$$a = [(5/2)\langle r^2 \rangle]^{1/2} , \tag{3.7}$$

and the effective radius along the axis of symmetry as

$$c = [5(\langle z^2 \rangle - \langle z \rangle^2)]^{1/2} . \tag{3.8}$$

The numerical factors 5/2 and 5 have been inserted in the definitions of a and c, respectively, so that they are the correct radii for a uniform ellipsoid. The aspect ratio of the cloud is then c/a. The mean density of the cloud is $\langle \rho_c \rangle = m_c/V_c$, where V_c is the total volume occupied by cloud material. We have found that it is difficult to calculate the mean density accurately for $\chi > 10$ because at late times a significant fraction of the cloud mass is in zones that contain both cloud and intercloud material (see § 8); our code treats the mass in these zones almost exactly (see Paper II), but it is less accurate in determining the fraction of the volume occupied by cloud material in a mixed zone. The tables also give the cloud velocity relative to the shocked intercloud medium, v_c', and the velocity dispersion in the axial and radial directions, δv_z and δv_r, all normalized to the blast wave velocity v_b. Finally, they list the integrated vorticity (the circulation), $\Gamma = \int \boldsymbol{\omega} \cdot \boldsymbol{dA}$.

4. MACH SCALING

The conditions behind a strong shock are virtually independent of the sound speed ahead of the shock, and this suggests that there should be a simple relationship among the cases run at different values of the Mach number $M = v_b/C_0$. The shock jump conditions give (Landau & Lifshitz 1959)

$$\rho_1 = \frac{(\gamma + 1)\rho_0}{(\gamma - 1) + 2M^{-2}} , \tag{4.1}$$

$$P_1 = \frac{2}{\gamma + 1} \rho_0 v_b^2 \left(1 - \frac{\gamma - 1}{2\gamma M^2}\right) , \tag{4.2}$$

so that for $M \lesssim 10$ the postshock density ρ_1 is within a few percent, and the postshock pressure P_1 is within a fraction of a percent, of their values at $M \to \infty$. Now note that the hydrody-

namic equations are invariant under the transformation

$$t \to tM\ , \quad v \to v/M\ , \quad P \to P/M^2\ , \tag{4.3}$$

with the position and density left unchanged. If in addition we choose to keep the upstream sound speed C_0 unchanged, then, so long as we can neglect the terms of order M^{-2} in the jump conditions, the transformed state will be the same for all Mach numbers. As a result, provided that $M \gg 1$, the time evolution of the cloud should be independent of the Mach number of the shock when expressed in terms of $t/t_{cc} \propto tv_b \propto tM$.

Table 2 shows that this expectation is borne out reasonably well. Comparison of the global quantities for the cases $M = 10$ and $M = 1000$ at a resolution of R_{120} shows that they agree to within 15% at the end of the calculation at $t = 5.05t_{cc}$. The morphology of the shocked cloud also provides a sensitive, albeit less quantitative, test of the scaling argument. Figure 2 shows the isodensity contours for the $M = 10$ and $M = 1000$ cases of the $\chi = 10$, $\gamma_c = 5/3$ problem at a time $t = 2.95t_{cc}$. Although the cloud has undergone substantial distortion due to Rayleigh-Taylor and Kelvin-Helmholtz instabilities, the agreement between the two cases is remarkable. We conclude that Mach scaling is valid: the evolution of the shocked cloud as a function of the normalized time t/t_{cc} is independent of the Mach number of the shock for large M.

5. OVERALL DESCRIPTION OF THE SHOCKED CLOUD

Four stages can be identified in the interaction of a shock with a cloud (Nittman et al. 1982; Heathcote & Brand 1983; McKee 1988). (1) There is an *initial transient* when the blast wave first strikes the cloud, sending a shock into the cloud and reflecting a shock back into the intercloud medium. The reflected shock settles into a standing bow shock or bow wave in a time of order $a/v_b = t_{ic}/2$. (2) The next stage is *shock compression:* After a time of order t_{ic}, the flow around the cloud converges on the axis behind the cloud, producing a high-pressure reflected shock in the intercloud medium and driving a shock into the rear of the cloud (Woodward 1976). The shocks compressing the cloud from the sides are weaker than those at the front and back of the cloud because the pressure is a minimum at the sides (Nittman et al. 1982). The result is that the cloud is compressed into a thin pancake, with its transverse dimension reduced by about a factor of 2. The collision of the main shock propagating in from the front of the cloud with the shock coming from the rear produces yet greater compression. (3) The *reexpansion* stage is initiated when the main cloud shock reaches the rear of the cloud, causing a strong rarefaction to be reflected back into the cloud and leading to an expansion of the shocked cloud downstream (Woodward 1976). At the same time, the low pressure at the sides of the cloud compared to that on the axis causes the cloud to expand laterally (Nittman et al. 1982). The lateral expansion continues to a time t_m, which is a few cloud crushing times. (4) The final stage is *cloud destruction*, as instabilities and differential forces due to the flow of the intercloud gas past the cloud cause it to fragment. This stage overlaps the previous one.

TABLE 2

MACH SCALING ($\chi = 10$, $\gamma_c = 5/3$, R_{120})

Parameter	$M = 10$	$M = 1000$
Time-independent Parameters		
v_{c0}/v_b	0.742	0.750
t_{drag}/t_{cc}	2.58	2.56
t_{dest}/t_{cc}	3.79	3.72
t_m/t_{cc}	3.70	4.45
Parameters at $t = 5.05t_{cc}$		
a/a_0	2.42	2.76
c/a_0	2.67	2.53
c/a	1.10	0.92
$\langle\rho_c\rangle/\rho_{c0}$	2.18	2.21
$\langle v_z\rangle/v_b$	0.093	0.089
$\delta v_z/v_b$	0.15	0.15
$\delta v_r/v_b$	0.094	0.102
$\Gamma/a_0 v_b$	1.86	1.82

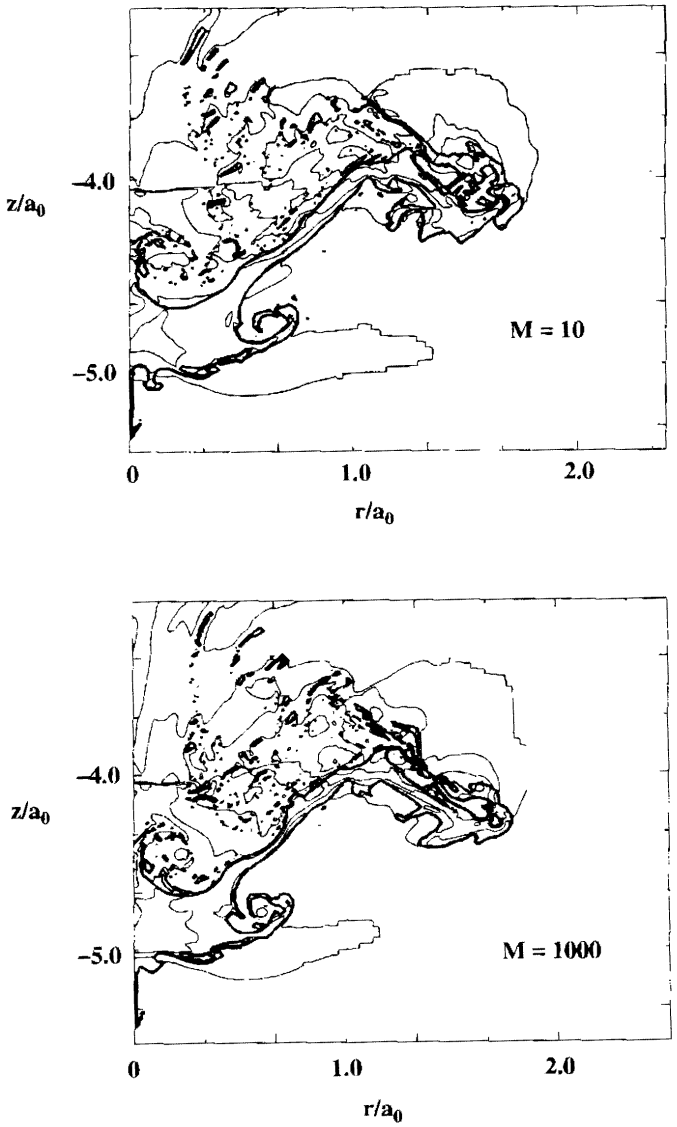

FIG. 2.—Mach scaling. At $t = 2.95t_{cc}$, the density contours indicate that the morphology of the shocked cloud is essentially the same for $M = 10$ and $M = 1000$.

5.1. *Evolution of the Pressure and Density*

When the blast wave strikes the cloud, it drives a shock into the cloud—the main cloud shock. It has been conjectured that the pressure behind this shock is initially about 6 times the pressure in the shocked intercloud medium, as would be expected for the reflection of a strong shock from a rigid

surface (Spitzer 1982; McKee 1988). Such a high pressure has not been seen in our simulations or in those of Bedogni & Woodward (1990). This high pressure is expected to persist only so long as the flow is approximately one-dimensional. It is possible that this approximation is satisfied for such a brief time that it did not show up in the output, which is sampled at discrete time intervals.

As the blast wave sweeps around the cloud, the flow in the intercloud medium settles into a steady state (McKee & Cowie 1975). Several pressures must be distinguished: the pressure in the shocked intercloud medium far from the cloud, P_i, which approaches $\frac{3}{4}\rho_{i0} v_b^2$ for strong shocks; the pressure at the stagnation point at the nose of the cloud, P_{st}; and the pressure just behind the main cloud shock, P_{c1}. We define the quantities F_{st} and F_{c1} by the relations

$$P_{st} \equiv F_{st} P_i , \tag{5.1}$$

$$P_{c1} \equiv F_{c1} P_{st} = F_{c1} F_{st} P_i . \tag{5.2}$$

The factor F_{st} exceeds unity so long as the shocked intercloud gas is flowing past the cloud. For a strong blast wave ($M \gg 1$) impinging on a dense cloud ($\chi \gg 1$), this factor is approximately

$$F_{st} \simeq 1 + \frac{2.16}{1 + 10.7[(\gamma_c + 1)\chi]^{-1/2}} \tag{5.3}$$

(McKee et al. 1987). On the other hand, the factor F_{c1} equals unity for a steady, plane shock; it exceeds unity if the cloud shock is decelerating, and is less than unity if the cloud shock is accelerating. Since the shock jump conditions give $P_{c1} = 2\rho_{c0} v_s^2/(\gamma_c + 1)$ for a strong shock, the velocity of the main cloud shock can be expressed in terms of the factors F_{st} and F_{c1} as

$$\frac{v_s}{v_b/\chi^{1/2}} \simeq \left(\frac{\gamma_c + 1}{8/3}\right)^{1/2} (F_{c1} F_{st})^{1/2} . \tag{5.4}$$

Recall that in the discussion in § 2 we took the right-hand side of this equation to be unity.

The numerical results show that, remarkably enough, the main cloud shock is almost planar, which simplifies analytic modeling. Our numerical results, as well as those of Bedogni & Woodward (1990), show that the actual value of the stagnation pressure is about 20% higher than the analytic estimate in equation (5.3). The numerical results also show that the factor F_{c1} is about 1.3, corresponding to a decelerating shock. With this value of F_{c1} and with the observed value of F_{st}, both our numerical results and those of Bedogni & Woodward (1990) are consistent with equation (5.4); the right-hand side of the equation is in the range 1.6–2.1 for $\chi > 10$ and $\gamma_c = 5/3$.

As the blast wave engulfs the cloud, it drives a weaker shock into the sides of the cloud. When this shock interacts with the main cloud shock, a third shock is created which deflects the gas that has passed through the side shock. These three shocks intersect at a triple point. There is a contact discontinuity with a velocity shear between the once-shocked gas and the twice-shocked gas; the vorticity associated with this velocity slip is generated at the triple point (see § 7).

The initial transient in the intercloud medium begins with the reflection of the blast wave shock from the cloud. The velocity of the shocked intercloud gas relative to the shocked cloud is comparable to the sound speed of the shocked intercloud gas, $0.56 v_b$. As a result, the reflected shock soon settles into a bow wave rather than a bow shock. A small amount of sound energy is radiated into the intercloud medium during this interaction (Spitzer 1982), but we have not attempted to measure it. After crossing the cloud, the intercloud shock converges behind the cloud at a time $\simeq 0.94 t_{cc}$, marking the end of the initial transient. In terms of the intercloud crossing time $t_{ic} = 2a_0/v_b$ defined in § 2.1, the shock convergence occurs at $1.5 t_{ic}$; this value applies to other values of χ as well.

When the intercloud shock first converges on the axis, it does so at normal incidence, and a strong reflected shock is formed. However, as the point of convergence moves away from the rear of the cloud, the angle at which the shock meets the axis becomes increasngly oblique. Eventually, the reflected shock interacts with the incident shock to produce a Mach reflected shock that propagates along the axis. (This is actually a double Mach reflected shock, with two triple points; see Glaz et al. 1985 and Hornung 1986.) The time resolution of our output is not adequate to pinpoint the moment at which the Mach reflected shock first forms, but it is clearly evident by $t = 1.05 t_{cc}$. A powerful supersonic vortex ring forms just behind the Mach reflected shock and is carried away from the cloud (see § 7.2). Note that the material in this vortex ring is advected downstream at a velocity faster than the shocked intercloud velocity $\frac{3}{4} v_b$, since it remains just behind the blast wave shock. The Mach reflected shock is quite strong, straightening out the blast wave shock in a time of order $v_b/a_0 = t_{ic}/2$. The pressure behind this shock is time-dependent; we have measured it to be as large as $1.65\rho_{i0} v_b^2$, compared with the pressure behind the unperturbed blast wave, $\frac{3}{4}\rho_{i0} v_b^2$. This high pressure drives a strong shock into the rear of the cloud, and this rear shock collides with the main cloud shock at a time $\sim 1.25 t_{cc}$. If we approximate this collision as occurring between two shocks of equal strength, then it is equivalent to a regular shock reflection at a fixed boundary. Since the shocks are strong, this collision increases the pressure in the shocked cloud to

$$P_{max} = \frac{3\gamma_c - 1}{\gamma_c - 1}\left(\frac{2}{\gamma_c + 1}\right)\rho_{c0} v_s^2 \tag{5.5}$$

(Landau & Lifshitz 1959), its maximum value. For $\gamma_c = 5/3$, this pressure is 6 times the pressure behind the main cloud shock. The corresponding maximum density is

$$\rho_{c,max} = \frac{\gamma_c}{\gamma_c - 1}\left(\frac{\gamma_c + 1}{\gamma_c - 1}\right)\rho_{c0} , \tag{5.6}$$

which is 2.5 times the density behind the main cloud shock for $\gamma_c = 5/3$. As shown in Figure 3, the mean cloud pressure reaches a maximum at this epoch.

When these shocks reach the cloud surface, rarefaction waves propagate back into the cloud and the reexpansion stage commences. At the point of maximum compression ($t \simeq 1.25 t_{cc}$), the shocks have flattened the cloud to the point that the diameter along the axis is about half that in transverse direction. Much of the cloud, having been shocked to a pressure $\sim 3\rho_{i0} v_b^2$, expands almost freely back into the shocked intercloud medium. The expansion in the radial direction slows substantially by $t_m \simeq 3.8 t_{cc}$. At this point, the shocked cloud is close to pressure equilibrium with the shocked intercloud medium (Fig. 3). The final value of the mean density of the shocked cloud can be estimated by assuming that the gas expands at constant entropy from the pressure and density in equations (5.3) and (5.4) to the pressure of the shocked inter-

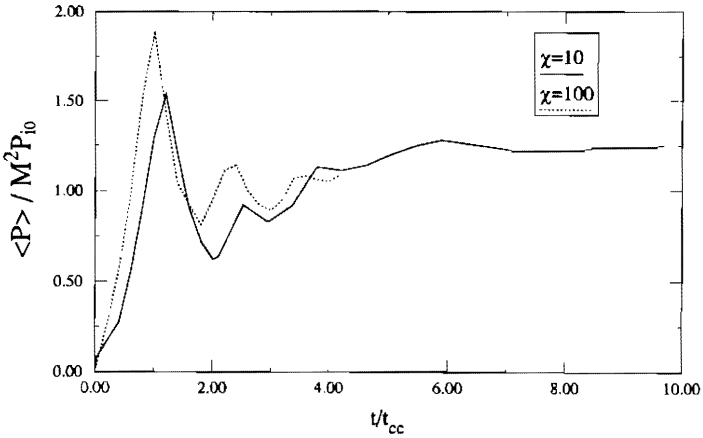

FIG. 3.—Time evolution of the mean cloud pressure for $\chi = 10$, 100 and $M = 10$. The pressure reaches a maximum at about t_{cc}, following the collision of the main cloud shock with the shock driven in from the rear of the cloud. For $t \gtrsim 4t_{cc}$ the shocked cloud is in approximate pressure equilibrium with the shocked intercloud medium.

cloud medium,

$$\langle \rho_{c,\mathrm{final}} \rangle \simeq \frac{\gamma_c(\gamma_c + 1)}{(\gamma_c - 1)^2} \left[\frac{\gamma_c - 1}{(3\gamma_c - 1)F_{c1}F_{\mathrm{st}}} \right]^{1/\gamma_c} \rho_{c0} \quad (5.7a)$$

$$\rightarrow \frac{3.41}{(F_{c1}F_{\mathrm{st}})^{3/5}} \rho_{c0} \quad \left(\gamma_c = \frac{5}{3}\right). \quad (5.7b)$$

The numerical calculations are consistent with this result: For the standard case ($\chi = 10$, $M = 10$), the calculations give $F_{c1}F_{\mathrm{st}} \simeq 2.6$, which implies $\langle \rho_{c,\mathrm{final}} \rangle = 1.92\rho_{c0}$; the numerical value of the mean density is close to this, $\langle \rho_{c,\mathrm{final}} \rangle \simeq 2.13\rho_{c0}$ (see Fig. 4). As discussed in § 3 above, it becomes increasingly difficult to determine accurately the mean cloud density from the numerical calculations at higher values of χ. The analytic estimate in equation (5.7) shows that the mean density declines slowly with χ, so that, for example, $\langle \rho_{c,\mathrm{final}} \rangle / \rho_{c0}$ is 1.2 times smaller at $\chi = 100$ than at $\chi = 10$.

One would have naively expected a shocked, adiabatic cloud to wind up at a density about 4 times higher than its initial density. The fact that the final density is about half this means that the radiative losses from the shocked cloud are smaller than would have been expected (see Mac Low et al. 1994). In particular, the constraint set on the shock velocity by the requirement that the shock be nonradiative (§ 2.3.1) can probably be relaxed somewhat, but calculations that include radiative losses are needed to determine by how much.

Cloud destruction proceeds in tandem with the reexpansion. The Richtmyer-Meshkov instability (Richtmyer 1960) contributes to this destruction. This instability, which is due to the impulsive acceleration of the cloud-intercloud boundary, grows linearly with time, rather than exponentially as does the Rayleigh-Taylor instability. Hence, it is important only if there are significant perturbations in the surface. In our problem, these perturbations are provided by the mesh; as the resolution increases, these perturbations become small and the Richtmyer-Meshkov instability becomes unimportant. However, it should be borne in mind that real clouds are not smooth, so this instability could play a role in nature. The dominant destruction mechanism of the cloud appears to be the Kelvin-Helmholtz and Rayleigh-Taylor instabilities. As discussed in § 2.1, these instabilities have growth times of order t_{cc}, and the effects of the instabilities are evident by $2.5t_{cc}$ (Fig. 5). By $3.8t_{cc}$, the cloud consists of a distorted, axially flattened core with a plume of fragments that contains over 70% of the mass of the cloud extending behind and to the side of the cloud (Fig. 5). A prominent shear layer exists due to the motion of the cloud through the intercloud medium. Vortex rings are apparent along this layer; note that they coincide with regions of severe cloud fragmentation (Fig. 6). The fragmentation of the cloud will be discussed further in § 8. By $t = 9.6t_{cc}$ (Fig. 7), the cloud is completely fragmented; it occupies a volume with about twice the transverse dimension and 5 times the axial dimension of the initial cloud, with no single fragment having more than 2% of the initial cloud mass.

5.2. *Scaling with Density Ratio* χ

As discussed in § 1, the cloud-shock interaction for small, nonradiative clouds depends on two parameters, the Mach number M and the density contrast χ. Table 3 shows the dependence on χ. Four models have been computed, with $\chi = 3$, 10, 30, and 100, all at a resolution of R_{120}. (One very high density case, with $\chi = 400$, was computed at R_{60}, but the

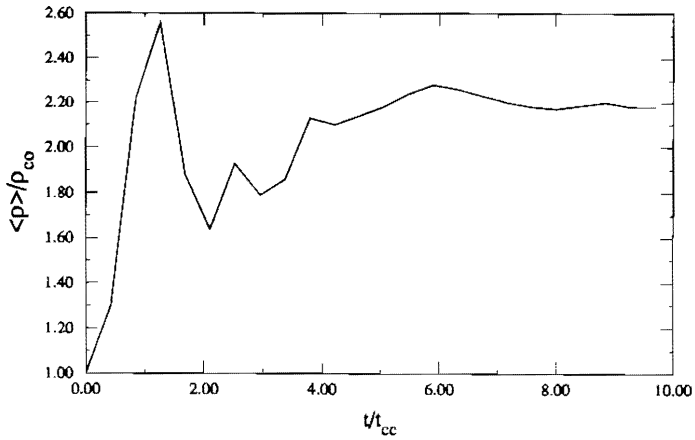

FIG. 4.—Time evolution of the mean cloud density for the standard case, $\chi = 10$, $M = 10$.

TABLE 3

χ SCALING ($M = 10$, $\gamma_c = 5/3$, R_{120})

Parameter	$\chi = 3$	$\chi = 10$	$\chi = 30$	$\chi = 100$
Time-independent Parameters				
C_c/v_b	0.323	0.177	0.102	0.056
t_{drag}/t_{cc}	1.53	2.58	2.96	3.79
t_{dest}/t_{cc}	8.16	3.79	3.17	3.90
t_{mix}/t_{cc}	>10	5.13	3.93	3.91
t_m/t_{cc}	4.00	3.70	3.90	4.20
Parameters at $t = t_m$				
a/a_0 [a]	1.44	2.26	3.03	3.21
c/a_0	0.94	1.61	2.55	8.39
c/a	0.65	0.71	0.84	2.62
$\langle \rho_c \rangle / \rho_{c0}$ [a]	2.75	2.13	...	...
$\langle v_z \rangle / v_b$	0.107	0.105	0.148	0.24
$\delta v_z/v_b$	0.119	0.185	0.187	0.22
$\delta v_r/v_b$	0.106	0.122	0.116	0.082
$\Gamma/a_0 v_b$ [a]	0.83	1.73	2.98	7.83

[a] This quantity is within about 10% of its asymptotic value at $t = t_m$.

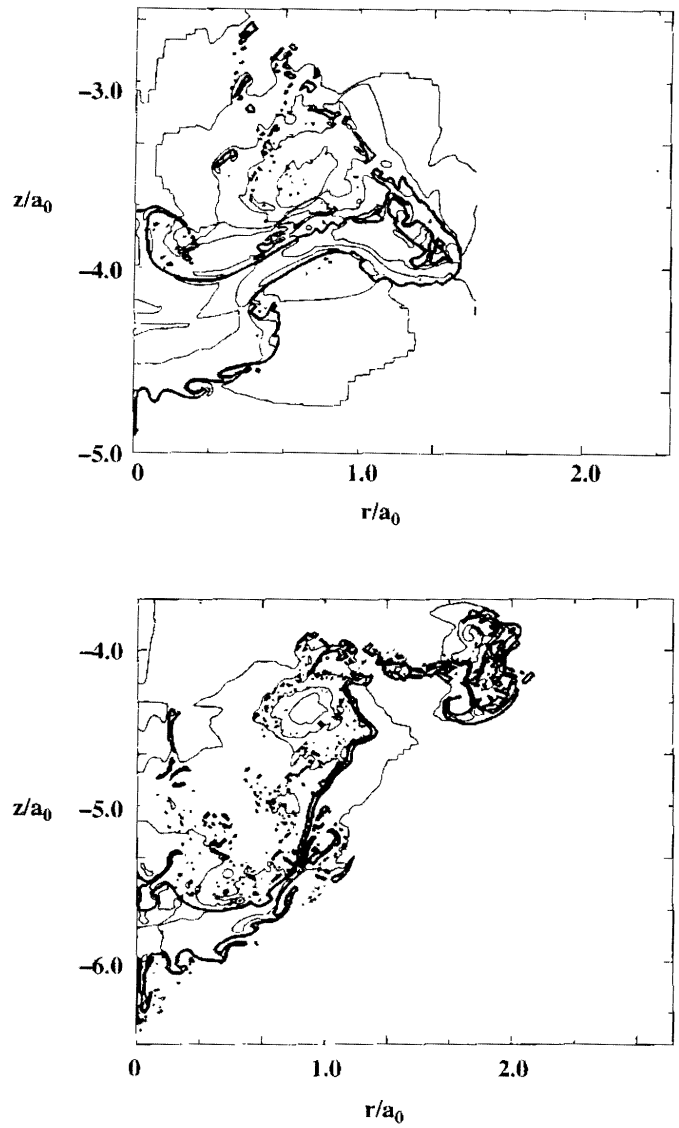

FIG. 5.—Density contours for the shocked cloud in the standard case. *Upper panel*: $t = 2.5t_{cc}$; *lower panel*: $t = 3.8t_{cc}$.

calculation was not continued to t_m.) To lowest order, we expect the time evolution to scale with the cloud crushing time t_{cc}, since the dynamical time scale of the shocked cloud and the instability growth times are all of order t_{cc} (see § 2.1). The table bears this out, but reveals that there are weak, but significant, deviations from this simple scaling. These differences can be attributed to the fact that the initial timescale for cloud drag does not scale with t_{cc} but rather scales with $\chi^{1/2}t_{cc}$ (eq. [2.6]); correspondingly, the velocity imparted to the cloud by the initial cloud shock scales as $\chi^{-1/2}$. As a result, the normalized drag time t_{drag}/t_{cc} increases weakly with χ. Because the Kelvin-Helmholtz instability and the Rayleigh-Taylor instability both depend on the relative velocity of the cloud and intercloud medium, the higher relative velocities at high χ lead to somewhat faster growth rates, thereby causing the normalized destruction time t_{dest}/t_{cc} to decrease weakly with χ. The numerical results show this decrease for χ between 3 and 30. The increase in t_{dest}/t_{cc} in going from $\chi = 30$ to $\chi = 100$ could be due to the lack of robustness of our definition of t_{dest}: in some cases the determination of whether the largest fragment is indeed a single fragment or whether it should be counted as two fragments can depend on a small number of zones.

Some of the observable characteristics of the shocked clouds are portrayed in Figures 8–10. The initially spherical cloud is strongly compressed in the axial direction, but it undergoes a steady expansion thereafter (Fig. 8). The axial stretching increases with χ because the core of the cloud takes longer to decelerate. The radial compression is less, and the cloud subsequently expands to about $2a_0$ for both $\chi = 10$ and $\chi = 100$. The $\chi = 10$ case extends to a time of almost $10t_{cc}$, and it shows that the radial size of the cloud remains constant at late times, in sharp contrast with the axial size. It is this feature of the calculations that enables us to define the time t_m at which the expansion is within 90% of its maximum value. In both cases, the cloud becomes prolate at late times. There are no reports of such elongated structures in supernova remnants, although it should be borne in mind that these calculations, being energy-conserving, apply to X-ray–emitting structures, for which little high-resolution mapping is available.

The time evolution evolution of the velocity dispersion in both the axial and radial directions is given in Figures 9 and 10. For $\chi = 10$, the axial dispersion δv_z is generally in the range $(0.1–0.2)v_b$; the range is somewhat larger for $\chi = 100$. The radial velocity dispersion δv_r is smaller, generally being in the range $(0.06–0.16)v_b$ for both cases. Note that the radial velocity dispersion continues after the cloud has reached its final size in the radial direction, and therefore provides a direct observational measure of the vorticity in the shocked cloud.

5.3. *Dependence on* γ_c

Finally, we consider the effect of varying the equation of state of the cloud. By setting $\gamma_c = 1.1$, we can see some of the qualitative effects of radiative losses in the shocked cloud. Softening the equation of state reduces the velocity of the cloud shock slightly, since the pressure behind the cloud shock, which is fixed, is related to the cloud shock velocity by $P_{c1} = 2\rho_{c0}v_s^2/(\gamma_c + 1)$. More important, the softer equation of state leads to substantially greater compression: the transverse dimension is reduced by as much as a factor of 2.0 and the axial dimension by as much as a factor of 4.4, compared with factors of 1.2 and 2.3, respectively, for $\gamma_c = 5/3$. The reexpansion of the cloud occurs with the characteristic velocity of the shocked cloud, $0.22v_b/\chi^{1/2}$, substantially slower than for $\gamma_c = 5/3$ (see eq. [3.3]). As a result, the cross-sectional area is significantly less than for $\gamma_c = 5/3$, which implies that the drag is less, the relative velocity remains high, and the Kelvin-Helmholtz and Rayleigh-Taylor instabilities are more violent (compare Fig. 5 with Fig. 11). By $3.8t_{cc}$, the cloud consists of a main pencil-like core with 55% of the mass plus a plume of fragments with 45% of the mass; at this time, the $\gamma_c = 5/3$ cloud has only 30% of the mass in the core. The conditions at $6.75t_{cc}$ are compared with those for the standard case in Table 4. Note in particular the higher mean compression for this case, 7.1 versus 2.2 for the standard case. The higher density of the shocked cloud enables it to survive longer: the destruction time is $5.7t_{cc}$, compared to $3.8t_{cc}$ for $\gamma_c = 5/3$.

6. CLOUD DRAG

Recall from the discussion in § 2.1 that if the cross section of the shocked cloud remained constant, then the cloud would become comoving with the postshock flow in a time $t_{drag,0} \simeq \chi^{1/2}t_{cc}$. This is just the time needed for the cloud to sweep up a column density of intercloud material about equal to the initial

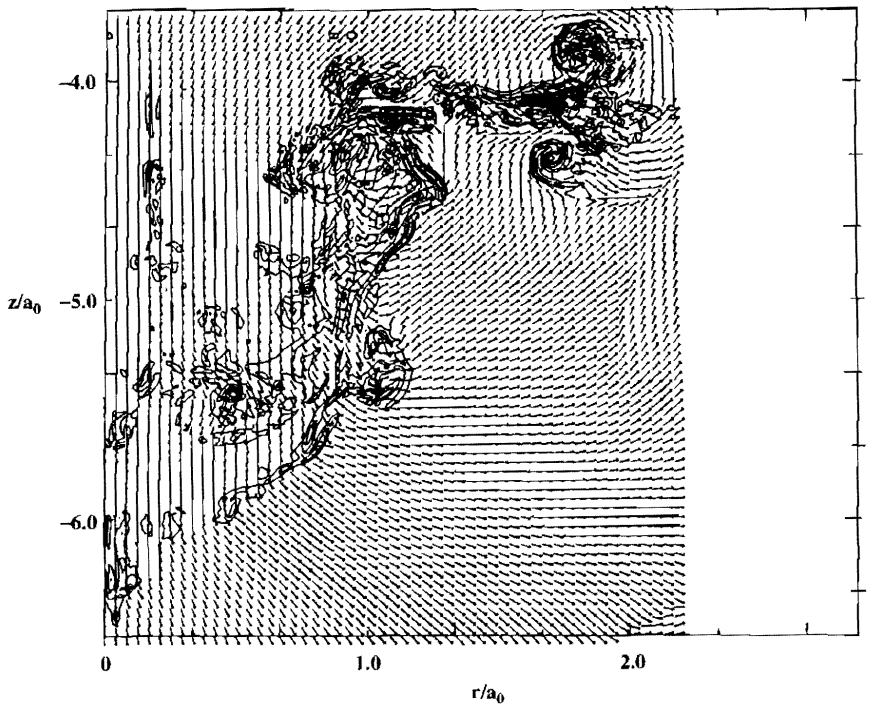

FIG. 6.—Vorticity contours and velocity direction vectors for the standard case at $t = 3.3t_{cc}$. Note the swirling motions associated with the large vortex ring in the upper right.

column density of the cloud, $n_0 v_b \chi^{1/2} t_{cc} = n_0 a_0 \chi = n_{c0} a_0$. In fact, the reexpansion of the shocked cloud substantially increases the drag and makes the drag time significantly less than $t_{drag,0}$. Let $a(t)$ be the transverse dimension of the cloud (Fig. 8*a*); initially, $a(0) = a_0$. For simplicity, we do not attempt to follow the reduction in a associated with the cloud compression. We assume that the cloud expands at the estimated sound speed of the shocked cloud, $\dot{a} \simeq C_c$ (see eq. [3.3]), until it reaches a maximum size at time t_m. However, since this reexpansion only begins after the cloud compression, we adopt

$$a(t) = [a_0^2 + (C_c t)^2]^{1/2} \quad (t \leq t_m) , \tag{6.1}$$

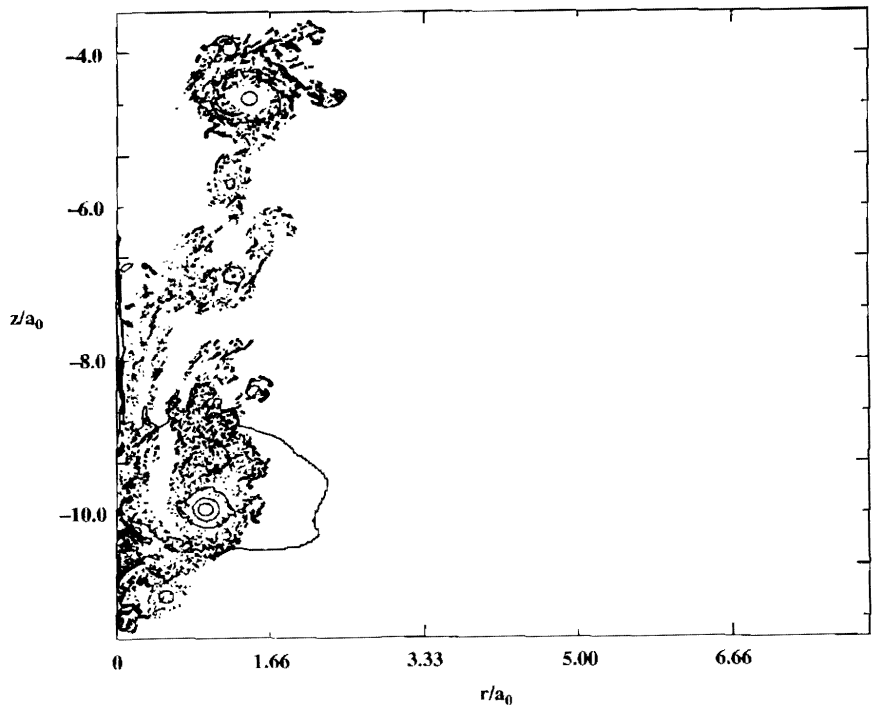

FIG. 7.—Density contours for the standard case at a late time ($t = 9.6t_{cc}$). The cloud is almost entirely torn up into small fragments. The circular structures visible at $z \simeq -10$ and $z \simeq -5$ are vortex rings; the density and pressure at the centers of the rings are quite small.

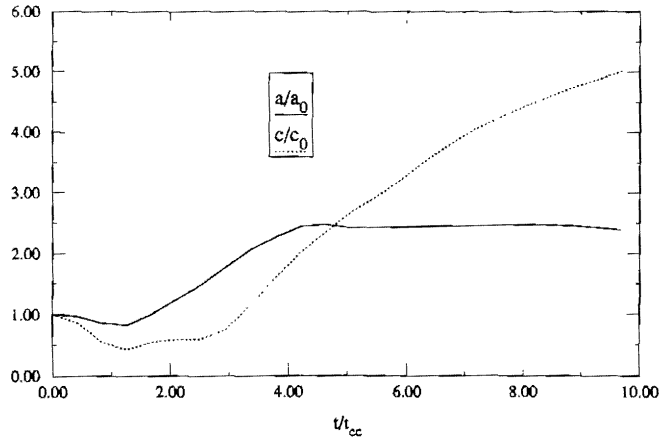

FIG. 8a

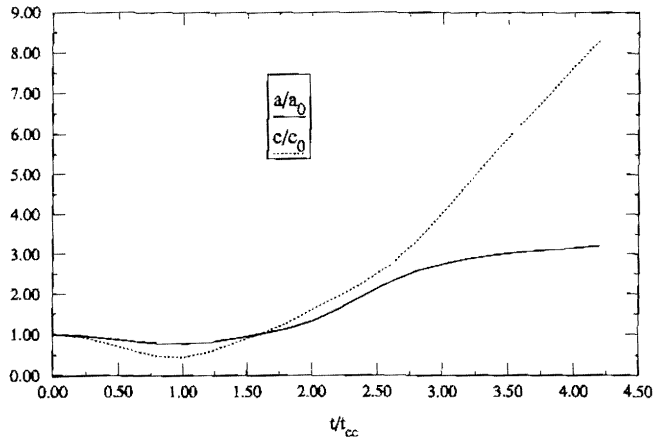

FIG. 8b

FIG. 8.—Time evolution of the cloud shape: the rms radial size a and the rms axial size c are plotted as functions of time. (*a*) Standard case: $\chi = 10$, $M = 10$. The radial size is within 10% of its maximum at $t_m = 3.70t_{cc}$ and thereafter remains about constant. The cloud switches from oblate to prolate at $4.8t_{cc}$. (*b*) $\chi = 100$, $M = 10$. The cloud is prolate for $t \gtrsim 1.6t_{cc}$.

which is less than the value that would be obtained by simply adding the expansion to the initial value. Inserting $A = \pi a(t)^2$ in the equation of motion of the cloud (eq. [2.5]) and noting that $|v_{c0}'| \simeq \frac{3}{4}v_b$ from equation (3.2), we find

$$\frac{v_c'}{v_{c0}'} = \left\{1 + \left(\frac{9}{8}\frac{C_D}{\chi^{1/2}}\right)\frac{t}{t_{cc}}\left[1 + \frac{1}{3}\left(\frac{C_c}{v_s}\frac{t}{t_{cc}}\right)^2\right]\right\}^{-1} \quad (t \le t_m) . \tag{6.2}$$

After the cloud ceases its expansion, the cloud velocity obeys

$$\frac{v_c'}{v_{c0}'} = \left\{1 + \left(\frac{9}{8}\frac{C_D}{\chi^{1/2}}\right)\left[\frac{t}{t_{cc}} + \left(\frac{C_c t_m}{v_s t_{cc}}\right)^2\left(\frac{t}{t_{cc}} - \frac{2}{3}\frac{t_m}{t_{cc}}\right)\right]\right\}^{-1} \quad (t > t_m) . \tag{6.3}$$

These equations describe three stages during the acceleration of the cloud: In the first stage ($t < t_m$, and the t^2 term in eq. [6.2] is negligible), the cloud area retains its initial value, and the characteristic drag time is $t_{drag,0}$. In this stage strong shocks traverse the cloud; the velocity given in equation (6.2) is the mass-weighted average. The second stage corresponds to the reexpansion stage of the shock-cloud interaction, in which the lateral expansion of the cloud increases the effective area of the cloud. This increase is represented by the term in square brackets in equation (6.2). For the typical case in which $\gamma_c = 5/3$, the factor $C_c/v_s = 0.56$ (eq. [3.3]), and this term is $1 + 0.104(t/t_{cc})^2$, so that the expansion has a major effect on the drag at a few cloud crushing times. If this stage were to

TABLE 4

DEPENDENCE ON γ_c ($\chi = 10$, $M = 10$, R_{120})

Parameter	$\gamma_c = 5/3$	$\gamma_c = 1.1$
Time-independent Parameters		
C_c/v_b	0.177	0.0706
t_{drag}/t_{cc}	2.58	5.44
t_{dest}/t_{cc}	3.79	5.69
t_m/t_{cc}	3.70	>6.75
Parameters at $t = 6.75t_{cc}$		
a/a_0	2.45	1.65
c/a_0	3.79	2.47
c/a	1.55	1.49
$\langle\rho_c\rangle/\rho_{c0}$	2.23	7.1
$\langle v_z\rangle/v_b$	0.087	0.192
$\delta v_z/v_b$	0.145	0.177
$\delta v_r/v_b$	0.082	0.096
$\Gamma/a_0 v_b$	1.86	2.50

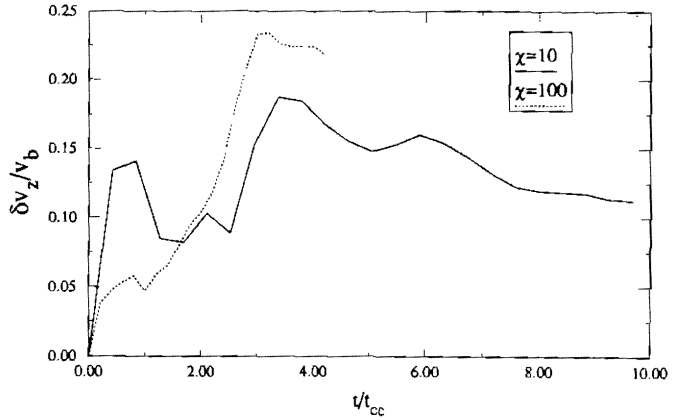

FIG. 9.—Axial velocity dispersion for $\chi = 10, 100$

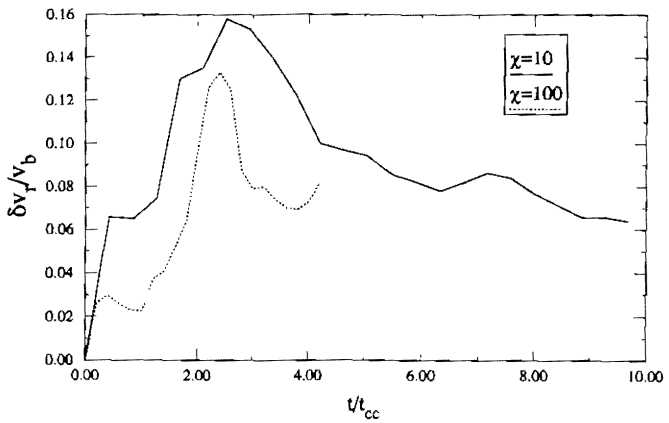

FIG. 10.—Radial velocity dispersion for $\chi = 10, 100$

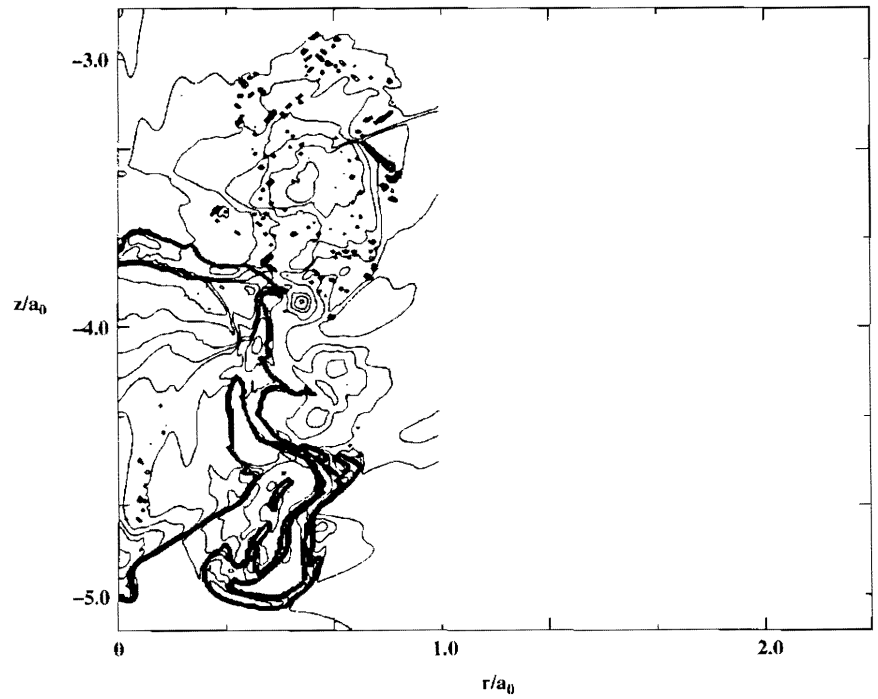

FIG. 11.—Density contours at $t = 2.52t_{cc}$ for a cloud with a soft equation of state ($\gamma_c = 1.1$), which simulates a radiative cloud shock

continue well beyond this time, then the velocity would scale as $(t/\chi^{1/6}t_{cc})^{-3}$, i.e., the characteristic time scale (in units of t_{cc}) would increase with density contrast as $\chi^{1/6}$. However, the reexpansion stops at $t_m \sim 4t_{cc}$, before this scaling can be established, and the final stage begins. Thereafter the relative velocity drops approximately as $1/t$, as is appropriate for a cloud of constant area.

This simple formulation of the cloud drag agrees reasonably well with the numerical results if we set the drag coefficient $C_D = 1$ (Fig. 12). In making this comparison, we use the mass-weighted velocity of *all* the cloud material, including that which has been stripped from the main cloud fragments. For $\chi = 10$, 30, 100, equation (6.2) is initially quite good, but as t approaches t_m the actual reduction in the cloud velocity becomes increasingly greater than the theoretical estimate, until the theoretical value of v_c' is too large by up to a factor of 1.5 (for $\chi = 10$) to 2 (for $\chi = 100$). However, the observed drag drops dramatically for $t \gtrsim t_m$, and theory and experiment converge soon thereafter. The longest run (in terms of cloud crushing times) is for the $\chi = 30$ case; for the time interval $5.85 < t/t_{cc} < 12.2$, the measured cloud velocity is within 12% of the value calculated from equation (6.3). At the end of this run, the relative cloud velocity drops to 7.7% of its initial value. For $\chi = 3$, the behavior is different: theory and numerical experiment agree to within a factor of 1.25 for $t < 5t_{cc}$, but for later times the numerical results show essentially no further deceler-

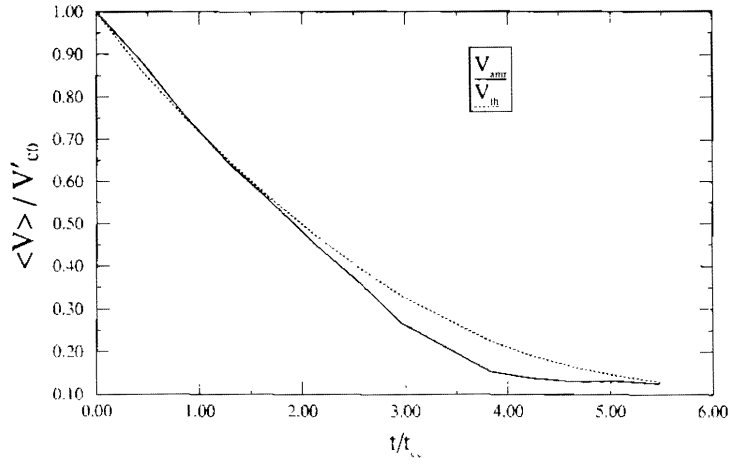

FIG. 12*a*

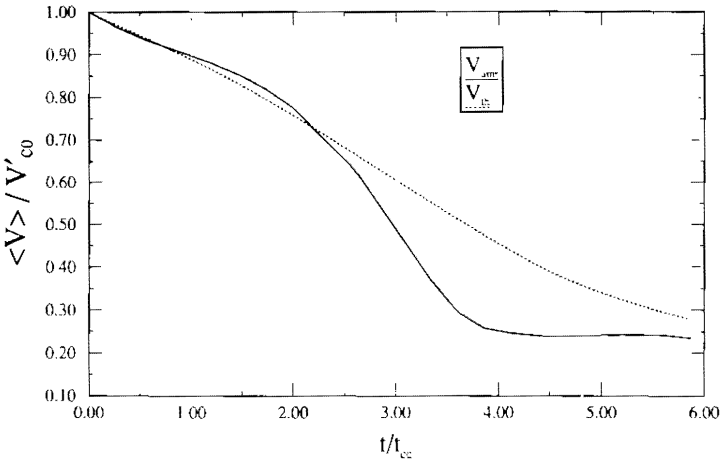

FIG. 12*b*

FIG. 12.—Cloud drag: comparison of theory (eqs. [6.2] and [6.3]) and numerical experiment for the mean cloud velocity as a function of time. (*a*) $\chi = 10$. (*b*) $\chi = 100$. Note that the theory underestimates the cloud deceleration (recall that the velocities are measured in the frame of the shocked intercloud medium) at intermediate times.

ation until the end of the run at $t = 10t_{cc}$, for reasons which are not clear. As a result, the difference between theory and experiment grows with time over this interval. In the opposite limit of a very dense cloud ($\chi = 400$), we were able to follow the evolution only out to $t = 2.3t_{cc}$, and we found agreement to within a few percent. Some of the discrepancy between theory and experiment is due to internal shocks in the cloud after the initial cloud crushing, an effect which we have not attempted to model. Given this limitation, the model for the drag appears reasonably successful.

Next, we apply the model to the cloud with the soft equation of state, $\gamma_c = 1.1$. In this case, the term in equation (6.2) that allows for the increase in cloud area is $1 + 0.0161(t/t_{cc})^2$. In contrast to the $\gamma_c = 5/3$ case, the model gives a cloud velocity v_c' that is too low by up to a factor of 1.35 for $t < t_m$.

7. VORTICITY

A striking aspect of the interaction of a shock wave with a cloud is the development of powerful vortex rings, which play an important role in the destruction of the cloud. It is well known that in an ideal fluid such as the one we are simulating, vorticity cannot be produced so long as the fluid is isentropic (or, more generally, so long as there is a one-to-one correspondence between P and ρ; Landau & Lifshitz 1959). Our problem differs from this case in two respects: the flow is not isentropic, both because of the initial conditions and because of the presence of shocks, and the inevitable presence of numerical viscosity due to the discretization of the partial differential equations means that the fluid is not ideal. We must demonstrate that the vorticity production in our simulations is not a numerical artifact. Yang et al. (1992) have made a numerical study of the vorticity generation at a shock-accelerated interface and have obtained good agreement both with experiment and with a theoretical model. Our problem differs from theirs in that we are considering a different geometry, and that we are interested in the high Mach number limit, where, as we shall see, simple analytic estimates are possible.

7.1. *Vorticity Production*

An illuminating form of the vorticity equation can be written as a mathematical identity. Let $\boldsymbol{\omega} \equiv \nabla \times \boldsymbol{v}$ be the vorticity, and let $\dot{\boldsymbol{v}}$ be the convective time derivative of the velocity $\boldsymbol{v}$. Then, with the aid of the vector identity

$$\boldsymbol{v} \times \boldsymbol{\omega} \equiv \tfrac{1}{2}\nabla v^2 - \boldsymbol{v} \cdot \nabla \boldsymbol{v} , \tag{7.1}$$

it is straightforward to show that

$$\frac{\partial \boldsymbol{\omega}}{\partial t} + \nabla \times (\boldsymbol{\omega} \times \boldsymbol{v}) \equiv \nabla \times \dot{\boldsymbol{v}} . \tag{7.2}$$

The left-hand side of this equation has the same form as the magnetohydrodynamic (MHD) equation for flux freezing if $\boldsymbol{\omega}$ is replaced by $\boldsymbol{B}$; we conclude that the vorticity is frozen into the fluid unless the acceleration has a curl. The circulation

$$\Gamma \equiv \int \boldsymbol{\omega} \cdot d\boldsymbol{A} \tag{7.3}$$

is analogous to the magnetic flux and satisfies the equation

$$\frac{d\Gamma}{dt} \equiv \int (\nabla \times \dot{\boldsymbol{v}}) \cdot d\boldsymbol{A} . \tag{7.4}$$

Note that since the vorticity is a curl, the circulation over a closed surface is zero. Furthermore, if the vorticity is spatially confined, then the circulation over an open surface extending beyond the region of nonzero vorticity is zero, since it is then possible to close the surface with a surface on which $\boldsymbol{\omega} = 0$. For the shock-cloud problem, the vorticity is confined to the vicinity of the cloud, so the circulation over any large plane cutting the cloud must be zero: the vorticity generated at any point is exactly canceled by that generated somewhere else.

To go from kinematics to dynamics, we must specify the acceleration. We allow for viscosity with a constant kinematic viscosity ν; this by no means represents the effects of an actual numerical viscosity, but it does allow us to get a feeling for the effects such a viscosity might have. For generality, we allow for a gravitational field $-\nabla\phi$ as well. The equation of motion for the fluid is then

$$\dot{\boldsymbol{v}} = -\frac{1}{\rho}\nabla P + \nu\nabla^2\boldsymbol{v} - \nabla\phi . \tag{7.5}$$

Inserting this in equation (7.2) yields the vorticity equation

$$\frac{\partial \boldsymbol{\omega}}{\partial t} + \nabla \times (\boldsymbol{\omega} \times \boldsymbol{v}) = \nabla P \times \nabla\left(\frac{1}{\rho}\right) + \nu\nabla^2\boldsymbol{\omega} . \tag{7.6}$$

The gravitational term has dropped out: gravity, being a potential field, cannot induce vorticity (Landau & Lifshitz 1959). There are two effects that can produce (or destroy) vorticity: a pressure gradient that is not aligned with the density gradient, and viscosity. If there are no solid boundaries in the problem, however, viscosity (at least in the simple form we have used to represent it) does not change the total circulation but only causes the vorticity to diffuse in space.

As we shall see, it is the first term on the right-hand side of equation (7.6), the baroclinic term, that is responsible for the production of the vorticity in the cloud-shock interaction (see also Picone & Boris 1988). An alternative form for this term can be obtained through use of the thermodynamic relation for the enthalpy per unit mass, $dw = T\,ds + dP/\rho$, where s is the entropy per unit mass:

$$\nabla P \times \nabla\left(\frac{1}{\rho}\right) = \nabla T \times \nabla s . \tag{7.7}$$

When inserted in equation (7.6), this relation immediately shows that the circulation is indeed conserved for isentropic flow of an ideal fluid. Shocks do not necessarily violate the conservation of circulation: planar shocks in a uniform medium do not generate an entropy gradient behind the shock and so produce no vorticity.

Let us now estimate the amount of vorticity produced by the shock-cloud interaction. As remarked above, the circulation over any large plane cutting the cloud vanishes, so we shall calculate the circulation in the half-plane bounded by the axis of symmetry ($r \geq 0$). First, consider the vorticity produced as the shock sweeps over the surface of the cloud. We shall assume that the cloud is dense ($\chi \gg 1$), so that we can ignore motion within it. The large difference in the acceleration of the fluid just outside the cloud compared with that inside gives a large curl to the acceleration and ensures that vorticity is generated (eq. [7.4]). While the shock is on the front side of the cloud, we may idealize the problem as follows: As the shock advances a distance dz parallel to the axis, it produces a shear over a distance $dz/\cos\theta$ along the surface of the cloud, where θ

is the angle at which the shock impacts the surface. The flow along the surface has a velocity $\frac{3}{4}v_b \cos\theta$, so the resulting vorticity is $\omega = -\frac{3}{4}v_b \cos\theta/h$, where h, the thickness of the shear layer, is related to the grid size in some fashion. (The minus sign is appropriate for the case in which v_z for the intercloud gas is greater than that for the cloud, as in Figure 1, since the vorticity then points in the $-\hat{\phi}$ direction). The rate of increase of circulation is then

$$\frac{d\Gamma}{dt} \simeq -\frac{3}{4}\left(\frac{v_b \cos\theta}{h}\right)\left(\frac{dz/\cos\theta}{dt}\right)h = -\frac{3}{4}v_b^2 . \quad (7.8)$$

The rate at which the circulation increases is independent of the size of the cloud. It is also independent of the uncertain value of the thickness of the shear layer h; the magnitude of the vorticity does depend on h, however, so we expect that it will depend on the resolution of the code. If we assume that the same result applies when the shock is passing over the rear of the cloud, we estimate that the total circulation produced by the shock sweeping over the cloud is $\Gamma \simeq (d\Gamma/dt)(1.5t_{ic})$, where $1.5t_{ic} = 3a_0/v_b$ is about equal to the time for the shock to pass the cloud according to the results described in § 5. Allowing for the fact that a finite value of the cloud/intercloud density ratio χ reduces the shear, and hence the circulation, by a factor of about $1 - \chi^{-1/2}$, we find

$$\Gamma_{\rm shock} \simeq -2.25 v_b a_0 (1 - \chi^{-1/2}) . \quad (7.9)$$

After the shock has swept over the cloud, vorticity continues to be generated by the baroclinic term,

$$\frac{d\Gamma}{dt} = \int \left(\nabla P \times \nabla \frac{1}{\rho}\right) \cdot d\boldsymbol{A} . \quad (7.10)$$

Now behind the shock the pressure is approximately constant across the boundary, but it does vary along the boundary, being a maximum at the stagnation point at the front of the cloud and smaller along the sides of the cloud. On the other hand, the variation of the density is primarily across the cloud boundary. We conclude that

$$\frac{d\Gamma}{dt} \simeq -\Delta P \,\Delta\left(\frac{1}{\rho}\right) \simeq -\frac{\Delta P}{\rho_i} \simeq -\frac{1}{2}v_c'^2 , \quad (7.11)$$

where we have estimated the average pressure drop as $\frac{1}{2}\rho_i v_c'^2$ (see § 2.1). Since the relative velocity of the cloud and the intercloud medium, v_c', is less than $\frac{3}{4}v_b$, it follows that the rate of increase of circulation due to the postshock flow over the cloud is smaller than that due to the shock itself by a factor of about $\frac{1}{2} \times \frac{3}{4} = \frac{3}{8}$. The total circulation produced by the postshock flow past the cloud can be estimated if we approximate the velocity of the cloud as $v_c' = v_{c0}' \exp(-t/t_{\rm drag})$. (A more accurate form for the cloud velocity has been given in § 6, but we shall see that this simple form suffices for our needs.) We then find

$$\Gamma_{\rm post} \simeq -\frac{1}{4}(v_{c0}')^2 t_{\rm drag} \quad (7.12a)$$

$$= -\frac{9}{64}\left(\frac{\chi^{1/2} t_{\rm drag}}{t_{cc}}\right) v_b a_0 , \quad (7.12b)$$

where expression (7.12b) is based on the strong shock result $v_{c0}' = -\frac{3}{4}v_b$.

Finally, we estimate the circulation associated with the supersonic vortex ring in the intercloud medium that is produced behind the cloud. In contrast to the cases considered above, this vorticity is not associated with the cloud boundary, and as a result it is advected away by the shock. When the shock sweeps over the cloud, it is delayed, so that a cusp forms on the axis with a radius of curvature of the order of the cloud radius a_0. The straightening of this cusp is associated with velocities of the order of the postshock flow velocity $\frac{3}{4}v_b$ over some transverse distance Δr, which results in a vorticity $+\frac{3}{4}v_b/\Delta r$. The sign of this vorticity is the opposite of that associated with the cloud boundary because in this case v_z increases toward the axis. Integrating over the area $\sim a_0 \Delta r$, we estimate that the circulation of the supersonic vortex ring is

$$\Gamma_{\rm ring} \simeq +\frac{3}{4}v_b a_0 . \quad (7.13)$$

An alternative derivation of this result, based on the fact that the vorticity is actually generated at the triple point associated with the Mach reflected shock (§ 5), provides additional physical insight. Because the shock has a finite thickness δs, the triple "point" actually occupies a finite area. The rate of production of circulation at the triple point depends on $\nabla \times \dot{v}$ according to equation (7.4). Now the acceleration across the shock is $\dot{v} \simeq \frac{3}{4}v_b/(\delta s/v_b)$. Let δh be the distance along the shock front over which the shock velocity changes direction in the vicinity of the triple point. Then, so long as there is a substantial angle between the blast wave shock and the Mach reflected shock, the curl is of order $\dot{v}/\delta h$. Integrating over the area of the triple "point" gives $d\Gamma/dt \simeq \frac{3}{4}v_b^2$; since the shock straightens out in a time $\sim a_0/v_b$, the total circulation is that given in the equation above. Note that this circulation has the opposite sign from that associated with the cloud boundary and is predicted to be somewhat smaller in magnitude than that produced by the shock, $\Gamma_{\rm shock}$ (eq. [7.9]).

Vorticity is produced in the cloud as well, but since the velocities in the cloud are smaller than those in the intercloud medium by a factor of order $\chi^{-1/2}$, the vorticity in the cloud is smaller by a similar factor. As discussed in § 5, at early times the main cloud shock and the side shock intersect at a triple point, and this generates vorticity as described above for the supersonic vortex ring. The sign of this vorticity is positive, since the flattening of the cloud implies that the material near the axis moves faster than that near the side. This vorticity is thus opposite in sign to that produced at the cloud-intercloud boundary. When the main cloud shock collides with the rear cloud shock, further vorticity is produced, but we have not attempted to follow that in detail.

To sum up, vorticity is produced by a curl in the acceleration (eq. [7.4]), which is proportional to the cross product of the pressure gradient and the density gradient (eq. [7.6]). This vorticity production can be broken down into four parts. Two are associated with the cloud-intercloud boundary and are produced by the initial passage of the shock ($\Gamma_{\rm shock}$; eq. [7.9]) and by the subsequent postshock flow ($\Gamma_{\rm post}$; eq. [7.12]). The third is entirely in the intercloud gas and is due to the triple points associated with the Mach reflected shocks behind the cloud ($\Gamma_{\rm ring}$; eq. [7.13]). Finally, there is vorticity in the cloud produced by the interaction of shocks there; it is smaller than that in the intercloud medium by a factor of order $\chi^{-1/2}$, so we have not considered it in detail.

7.2. *Comparison with Numerical Experiment*

In order to minimize the effects of the cloud vorticity, we first compare the theory to a calculation of the interaction of a blast wave with a dense cloud ($\chi = 100$, with $\mathcal{M} = 100$). Figure 13 shows that the magnitude of the circulation rises almost lin-

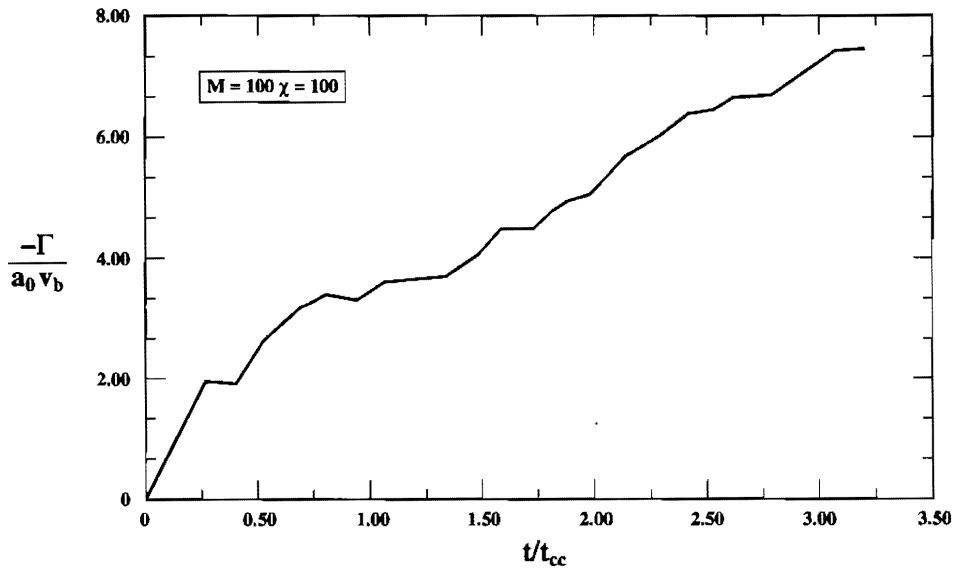

FIG. 13.—Total circulation as a function of time for $M = 100$, $\chi = 100$

early with time until $0.3t_{cc}$, where it reaches a value $\simeq -2v_b a_0$. At this point the blast wave shock reaches the axis behind the cloud (note that this time is $1.5t_{ic}$, as found in § 5), so we identify this circulation with Γ_{shock}, which is $-2.03v_b a_0$ according to equation (7.9). After shock convergence, a positive contribution to the circulation is observed. A plot of the axial distribution of the vorticity (Fig. 14) at $t = 0.77t_{cc}$ shows that this is associated with the supersoic vortex ring, and amounts to $+0.73v_b a_0$; by comparison, equation (7.13) gives $\Gamma_{ring} = +0.75v_b a_0$. The ring runs off the high-resolution part of the grid at $t \simeq 0.8t_{cc}$, and thereafter Γ_{ring} is not included in the total circulation plotted in Figure 13. The most dramatic aspect of the figure is the subsequent increase in the magnitude of the circulation until the end of the calculation at $t = 3.2t_{cc}$. The final value is $\Gamma = -7.5v_b a_0$. The magnitude of Γ is not expected to increase much beyond this, since the calculation has reached a time close to t_m and t_{drag}; a lower resolution calculation at R_{60} shows that $|\Gamma|$ increases by only about 10% from $3.2t_{cc}$ to $4.26t_{cc}$. Equation (7.12) shows that the postshock vorticity generation scales approximately as $\chi^{1/2}$ (since t_{drag}/t_{cc} is roughly constant) and therefore exceeds that generated by the shock at high χ. The sum of the two contributions, $\Gamma_{shock} + \Gamma_{post} = -6.7v_b a_0$, is in reasonably good agreement with the value obtained from the numerical simulations. (Note: The R_{120} calculation for this case ended before reaching the drag time, so we have used the R_{60} value for the drag time, $t_{drag} = 3.34t_{cc}$, to estimate Γ_{post}.) Overall, the agreement between theory and numerical experiment is within about 15% in this case.

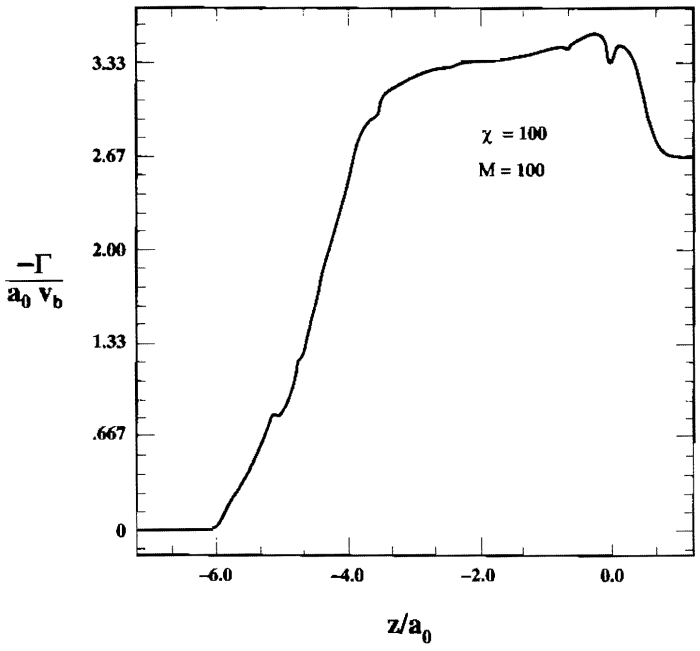

FIG. 14.—Circulation as a function of position at $t = 0.77t_{cc}$ for $M = 100$, $\chi = 100$: the vorticity is integrated from the bottom of the calculational volume ($z \simeq -7$) up to z. The positive contribution to the vorticity at $z > 0$ is due to the vortex ring just behind the blast wave shock.

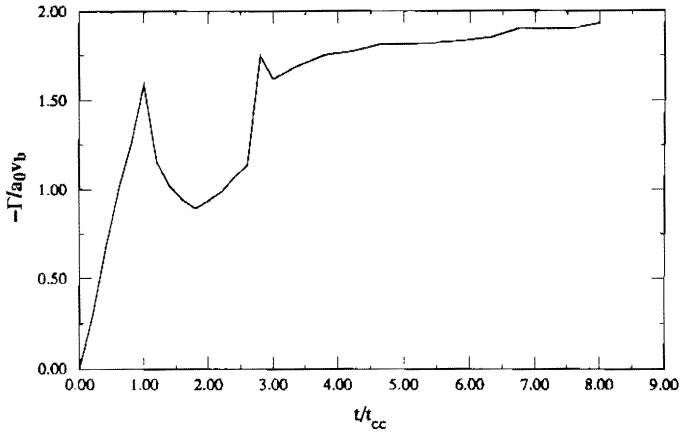

FIG. 15.—Total circulation as a function of time for the standard case. The formation of the supersonic vortex ring produces the positive contribution to the circulation which begins to appear at $t \simeq 1.0t_{cc}$.

Next, we consider the results at a lower value of the density contrast, $\chi = 10$. Figure 15 shows that the first peak in the circulation, which corresponds to that generated by the shock, is $\Gamma = -1.6 v_b a_0$, comparable to the value $-1.54 v_b a_0$ predicted by equation (7.9). The vorticity associated with the supersonic vortex ring can be read off from Figure 16, $+0.65 v_b a_0$; equation (7.13) gives $+0.75 v_b a_0$. The density and vorticity contour plots in Figure 16 show that the ring is located just behind the Mach disk, and that the density becomes extremely small in the ring. After the supersonic vortex ring has left the grid, the total circulation approaches $\Gamma \simeq -2.1 v_b a_0$ asymptotically; by comparison, theory predicts $\Gamma_{\rm shock} + \Gamma_{\rm post} = -2.7 v_b a_0$. The agreement between theory and numerical experiment is not as good as in the $\chi = 100$ case, as expected: we have not attempted to estimate the cloud circulation, which should reduce the total circulation by about $1 - \chi^{-1/2}$, or about 30%. These results confirm that the relative importance of the shock-generated circulation increases as the density contrast decreases. For yet smaller values of χ, the shock-generated circulation becomes dominant, as found by Picone & Boris (1988).

The simple model for vorticity generation in § 7.1 suggests that the only effect of changing the adiabatic index of the cloud gas is in $t_{\rm drag}$ (eq. [7.12]). The $\gamma_c = 1.1$ case described in § 5 has $t_{\rm drag} = 5.44 t_{\rm cc}$, substantially greater than that for $\gamma_c = 5/3$. As a result, the total circulation for $\gamma_c = 1.1$ is predicted to be larger than that for $\gamma_c = 5/3$ by a factor of 1.5. At $t = 6.74 t_{\rm cc}$, when the $\gamma_c = 1.1$ calculation was terminated, the measured circulation is 1.34 times greater than that for $\gamma_c = 5/3$, in rough agreement with the prediction.

The good agreement we have found between the simple theoretical model of vorticity generation in § 7.1 and the numerical results indicates that we have indeed identified the major sources of vorticity in the cloud-shock interaction. We therefore conclude that numerical viscosity does not have a significant effect on our calculation of the vorticity, consistent with the conclusion to be reached in Paper II on the basis of convergence studies.

Finally, we note that although the circulation is well determined by our calculations, the peak vorticity is not. The magnitude of the vorticity is governed by the thickness of the shear layer. For example, if the vorticity is generated at a triple point, then its magnitude is determined by the thickness of the shocks there, which (in most astrophysical applications, at least) are far too thin to be resolved by our calculation. Since the thickness of the simulated shock is of the order of the grid spacing Δx, we expect the peak vorticity to scale as $(\Delta x)^{-1}$, and we have confirmed this by measuring the peak vorticity as the shock sweeps over the cloud at resolutions ranging from R_{30} to R_{240} (see Paper II).

8. CLOUD FRAGMENTATION

The destruction of the shocked cloud is due to its fragmentation, on scales both large and small. This fragmentation is driven by Kelvin-Helmholtz and Rayleigh-Taylor instabilities, each of which has a characteristic growth time of the order of the cloud crushing time (§ 2). The Richtmyer-Meshkov instability also contributes to the fragmentation, but it is less important because it grows linearly rather than exponentially (see § 5.1). The time evolution of the mass spectrum of the fragments will be discussed in Paper II. Here we focus on two measures of the time it takes to destroy the cloud: the destruc-

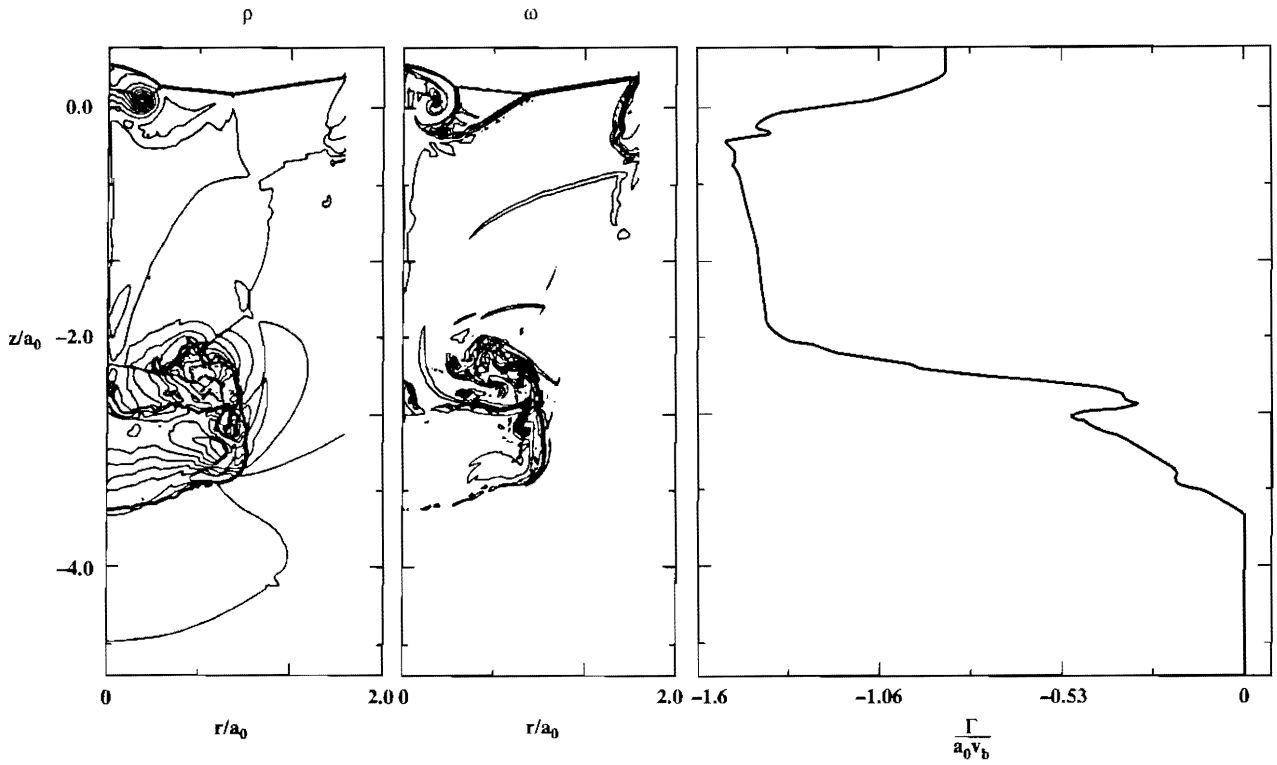

FIG. 16.—Matched density contours, vorticity contours, and circulation as a function of position at $t = 1.68 t_{\rm cc}$ for the standard case. Level 3 grids were permitted only out to a radius $1.67 a_0$, and the density and vorticity contours are restricted to this region. The vorticity in the upper right-hand corner of the vorticity panel is a numerical artifact associated with the change in the permitted resolution.

tion time, t_{dest}, which focuses on large-scale fragmentation, and the mixing time, t_{mix}, which focuses on small-scale fragmentation.

A shocked cloud develops a core-plume structure, in which some of the cloud mass is concentrated in a core near the axis while the remainder is stretched out behind the cloud in a plume (e.g., Fig. 5). The destruction time is defined as the time at which the mass of the core has been reduced to a fraction $1/e$ of the initial cloud mass. The core mass is defined as the mass of the gas that is physically connected to the main axial fragment. It can change discontinuously when the core splits into two fragments. Since the connection between the two parts of the cloud that ultimately break apart may be delineated by only a few zones, the determination of t_{dest} is sometimes affected by numerical artifacts. Our results show that for density ratios in the range $10 \lesssim \chi \lesssim 100$, the destruction time is $t_{dest} \simeq 3.5 t_{cc}$. During this time, the blast wave advances a distance

$$\Delta z_b(t_{dest}) = v_b t_{dest} \simeq 3.5 \chi^{1/2} a_0 . \quad (8.1)$$

Thus, for example, a cloud with $\chi = 10$ will be substantially destroyed by the time the blast wave advances 10 cloud radii.

It is a feature of the Kelvin-Helmholtz and Rayleigh-Taylor instabilities that, in the absence of viscosity, surface tension, magnetic fields, etc., there is no minimum length scale. As a result, we expect the fragmentation to occur down to the resolution of the code, in this case the third level zones of the AMR scheme. At this point, individual zones will contain both cloud and intercloud material. The fraction of the cloud mass in such zones is the "mix fraction," and the time at which the mix fraction reaches $\frac{1}{2}$ is the mixing time, t_{mix}. Despite the fact that the definition of the mixing time depends explicitly on the resolution of the code, convergence studies show that it is a well-defined quantity (Paper II). This makes sense physically: the fragmentation time is dominated by the growth rate of the instabilities on large scales (§ 2). As shown in Figure 17, mixing occurs more rapidly for larger χ. We attribute this to the higher relative velocity at higher χ (the drag time increases slowly with χ, as discussed in § 6), which decreases the growth time of both the Kelvin-Helmholtz and Rayleigh-Taylor instabilities, t_{KH} and t_{RT}. The velocity dependence of the Kelvin-Helmholtz growth time is apparent from equation (2.7), $t_{KH} \propto 1/v_{rel}$. The expression for Rayleigh-Taylor growth time in equation (2.8) applies to early times; more generally, with the aid of equation (2.5), we find that t_{RT} scales as $1/v_c' = 1/v_{rel}$ also. However, the growth rate of the Kelvin-Helmholtz instability scales directly with the wavenumber k, whereas the growth rate of the Rayleigh-Taylor instability scales as $k^{1/2}$; thus, the Kelvin-Helmholtz instability should dominate the small-scale fragmentation.

A simple hierarchical model for fragmentation by the Kelvin-Helmholtz instability can be developed by assuming that the cloud first fragments into a few large fragments of comparable mass, and that these in turn fragment into a several fragments of comparable mass, and so on. Such a process leads to the most rapid possible mixing, since it continually exposes the interior of the cloud to mixing. When the fragmentation is occurring at wavenumbers of order k, the growth time is given by equation (2.7). The time to advance to the next stage of the fragmentation is then

$$\frac{dt}{t_{cc}} \propto \frac{t_{KH}}{t_{cc}} d\ln k \simeq \left(\frac{v_{c0}'/v_c'}{k a_0}\right) d\ln k . \quad (8.2)$$

The distance the cloud travels in the frame of the shocked intercloud gas during the time it takes the cloud to fragment to very small scales ($k \to \infty$) is then

$$\Delta z_c' = \int v_c' dt \propto -\frac{v_b t_{cc}}{k_0 a_0} \propto -\chi^{1/2} a_0 , \quad (8.3)$$

where $k_0 \sim 2\pi/a_0$ is the wavenumber of the largest fragment. As shown in Figure 18, this $\chi^{1/2}$ scaling is satisfied quite well for $3 \le \chi \le 100$. The numerical coefficient as determined from our simulations yields

$$\Delta z_c'(t_{mix}) \simeq -1.68 \chi^{1/2} a_0 . \quad (8.4)$$

At the largest χ, the observed value of $\Delta z_c'$ is about 25% larger than this. This could be due to a change in the nature of the fragmentation at large χ: rather than initially breaking up into several large fragments, at large χ the core appears to undergo stripping from its surface, which is a less effective mixing mechanism. This shift is apparent in the relative values of the

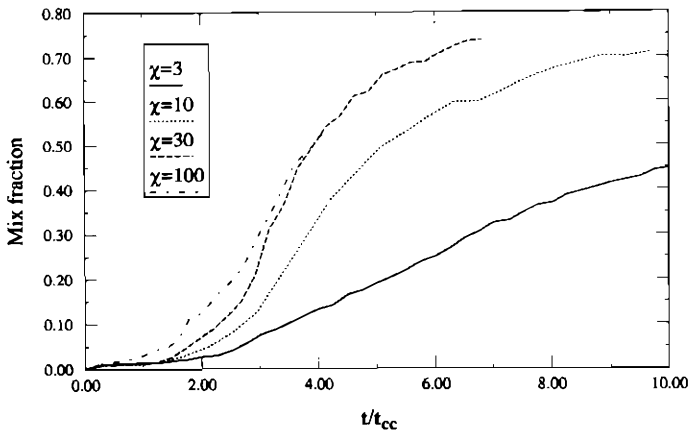

FIG. 17.—Mixing of cloud and intercloud material: fraction of the cloud mass that is located in individual level 3 zones as a function of time for several values of the density contrast χ. Half the cloud is mixed at the time t_{mix} given in Table 3.

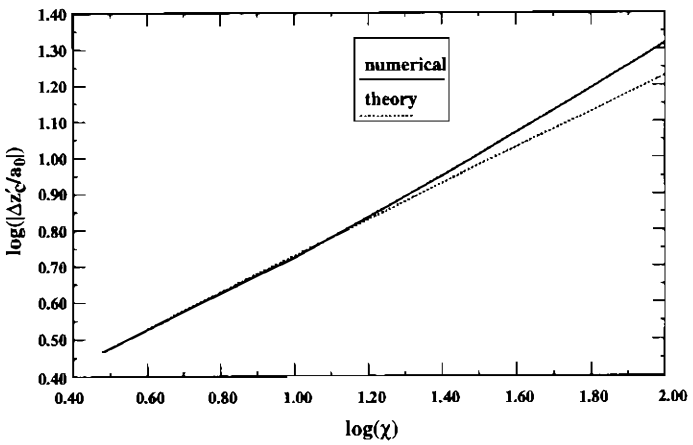

FIG. 18.—Comparison of theory (eq. [8.3]) and numerical experiment for the χ dependence of the mixing of cloud and intercloud material. $|\Delta z'|$ is the distance the cloud has moved at t_{mix} in the frame of the shocked fluid.

destruction time and the mixing time: for $\chi = 3$, 10, 30, large-scale fragmentation occurs before mixing ($t_{\rm dest} < t_{\rm mix}$), whereas at $\chi = 100$ the two processes occur at the same time. It remains to be seen whether this change in the nature of the fragmentation with χ persists in a three-dimensional calculation, since there are more modes of large-scale fragmentation in three dimensions than in two.

For comparison with observation, it is convenient to express distances in the frame of the unshocked intercloud medium, which often coincides with the observer's frame. Since the shocked intercloud medium is moving at a velocity $v_{i1} \simeq \frac{3}{4} v_b$, positions in the two frames are related by

$$\Delta z_c \simeq \Delta z_c' + \frac{3}{4} v_b t = \Delta z_c' + \frac{3}{4}\left(\frac{t}{t_{cc}}\right)\chi^{1/2} a_0 \ . \qquad (8.5)$$

In this frame, the distance the cloud has moved at $t_{\rm mix}$ does not scale as $\chi^{1/2}$; indeed, for $10 \lesssim \chi \lesssim 100$, the distance is roughly constant, with $\Delta z_c(t_{\rm mix}) \simeq (6\text{–}8) a_0$. Since the destruction time is no greater than the mixing time, this means that a small, non-radiative cloud can be displaced no more than about 8 cloud radii before being destroyed and mixed with the intercloud medium.

9. RELATED PROBLEMS

9.1. *Cylindrical Cloud*

In order to infer the generality of our results, we have considered two problems that are related to that of a spherical cloud struck by a blast wave. The first is to alter the geometry of the cloud from spherical to cylindrical. In discussing this problem, it is convenient to introduce a modification of the cloud crushing time t_{cc}. If the initial cloud is ellipsoidal, with a semimajor axis in the z-direction of c_0, then the solution of the cloud drag equation (eq. [6.2]) for $t < t_m$ becomes

$$\frac{v_c'}{v_{c0}'} = \left\{1 + \frac{9}{8}\frac{C_D}{\chi^{1/2}}\left(\frac{a_0}{c_0}\right)\frac{t}{t_{cc}}\left[1 + \frac{1}{3}\frac{C_c^2}{v_s^2}\left(\frac{t}{t_{cc}}\right)^2\right]\right\}^{-1} . \qquad (9.1)$$

It is clear from this expression that the dynamics of the shocked cloud depends on both dimensions of the cloud: the term proportional to t/t_{cc}, which measures the initial cloud drag, is multiplied by a factor a_0/c_0, which has the effect of normalizing the time with respect to $\chi^{1/2} c_0/v_b$; on the other hand, the term proportional to $(t/t_{cc})^2$ is independent of c_0. To capture the effects of the different dimensions in an approximate fashion, we introduce the modified cloud crushing time,

$$t_{cc}' \equiv \frac{(\chi a_0 c_0)^{1/2}}{v_b} . \qquad (9.2)$$

We have considered the case of a cylinder with an aspect ratio $c_0/a_0 = 3$, so that the modified cloud crushing time is $t_{cc}' = (3)^{1/2} t_{cc}$. In terms of this modified cloud crushing time, Table 5 shows reasonably good agreement between the results for the cylindrical cloud and those for the spherical cloud. (Note that the velocities in the table have been normalized with respect to v_{c0}' to facilitate comparison with the case of a cloud immersed in a wind; see § 9.2). For example, the destruction time for the cylindrical cloud is $4.64 t_{cc}'$, comparable to the value $3.79 t_{cc}$ for the spherical cloud. The principal difference between the two cases is the cloud shape, which is actually more flattened in the cylindrical case than in the spherical case. This is due to the enhanced radial expansion resulting from the small initial value of the radial dimension a_0 relative to that of the axial dimension c_0. We conclude that modest changes in the initial shape of the cloud do not alter our main conclusions on the shock-cloud interaction.

TABLE 5

RELATED PROBLEMS ($\chi = 10$, $\gamma_c = 5/3$, R_{120})

Parameter	Standard ($c_0 = a_0$)	Cylinder ($c_0 = 3a_0$)	Cloud-Wind ($4c_1 \simeq c_0 = a_0$)
Time-independent Parameters			
t_{cc}'/t_{cc}	1.00	$3^{1/2}$	1.00
$\lvert v_{c0}'\rvert/v_b$	0.742	0.742	0.505
$t_{\rm drag}/t_{cc}'$	2.58	3.29	3.79
$t_{\rm dest}/t_{cc}'$	3.79	4.64	6.15
t_m/t_{cc}'	3.70	4.38	6.17
Parameters at $t = t_m$			
a/a_0	2.26	3.50	1.60
c/a_0	1.61	1.94	2.27
c/a	0.71	0.55	1.42
$\langle\rho_c\rangle/\rho_{c0}$	2.13	1.61	3.33
$\langle v_z\rangle/\lvert v_{c0}'\rvert$	0.142	0.164	0.27
$\delta v_z/\lvert v_{c0}'\rvert$	0.25	0.26	0.24
$\delta v_r/\lvert v_{c0}'\rvert$	0.164	0.205	0.147
$\Gamma/(a_0 c_0)^{1/2} v_{c0}'$	2.33	2.19	2.99

NOTE.—v_{c0}' is the initial velocity of the cloud relative to the shocked intercloud medium for the standard case and the cylinder case. In the cloud-wind case, it is the initial velocity of the cloud relative to the shocked wind; v_b is the velocity of a hypothetical shock that would produce such a relative velocity.

9.2. *Cloud in a Wind*

A problem of considerable astrophysical interest is that of a cloud moving through an intercloud medium—i.e., a cloud in a wind. In general, the wind can have an arbitrary Mach number relative to the cloud. The flow of the shocked intercloud gas past the shocked cloud at a velocity v_{c0}' corresponds to the particular case of a wind with a Mach number v_{c0}'/C_i, where $C_i = 0.56 v_b$ for $\gamma_i = 5/3$. How would the cloud evolve if it were placed in such a wind without the initial shock?

To study this problem, we have attempted to model a cloud immersed in the flow behind a shock, but without the disruptive effects of the shock itself. The intercloud medium has the properties of the intercloud gas behind the blast wave shock (e.g., density ρ_{i1}). The cloud has the same mass and transverse radius (a_0) as the cloud in the shock-cloud problem. To facilitate comparison with the shock-cloud problem, the cloud is assumed to have been compressed from some hypothetical state in which its density was ρ_{c0} to a state in which its density is ρ_{c1}, which is χ times greater than that in the intercloud medium ($\rho_{c1} = \chi\rho_{i1}$) This definition of χ is equivalent to that in the shock-cloud problem, provided that $\gamma_c = \gamma_i$, so that $\rho_{c1}/\rho_{i1} = \rho_{c0}/\rho_{i0}$, and we assume that to be the case here. To make the column density of the cloud the same as in the shock-cloud problem, the uncompressed cloud must have had an axial radius $c_0 \simeq a_0$; as a result, the modified cloud crushing time t_{cc}' defined in equation (9.2) is the same as t_{cc}. At the beginning of the calculation, the cloud is a flattened ellipsoid with an axial radius $c_1 \simeq a_0/4$, so that its density is $\chi\rho_{i1}$. This initial cloud then qualitatively resembles the cloud after the passage of the blast wave. (In fact, we have chosen c_1/a_0 to match the value appropriate for a Mach 10 shock, which is 1/3.9.) We choose the initial relative velocity between the cloud and the wind, v_{c0}', to correspond to the velocity of the cloud in the shock-cloud problem after the passage of the blast wave;

for the case we consider, $\chi = 10$, this is $0.505v_b$, corresponding to an initial Mach number 0.90. Finally, we assume that the cloud has the same thermal pressure as the intercloud medium.

The main result of this exercise is that, despite the absence of the blast shock, the cloud is decelerated and destroyed in times that are only about 50% greater than in the shock-cloud case (Table 5 and Fig. 19). The initial conditions we have chosen result in both a bow shock and a transmitted shock because the system is not in dynamical equilibrium; such transient shocks are to be expected in the interaction of a wind with a cloud as the cloud adjusts to the conditions in the wind. The peak pressure in the cloud produced by these shocks is much less than that in the shock-cloud case, and the Mach reflected shock downstream from the cloud is also much weaker than

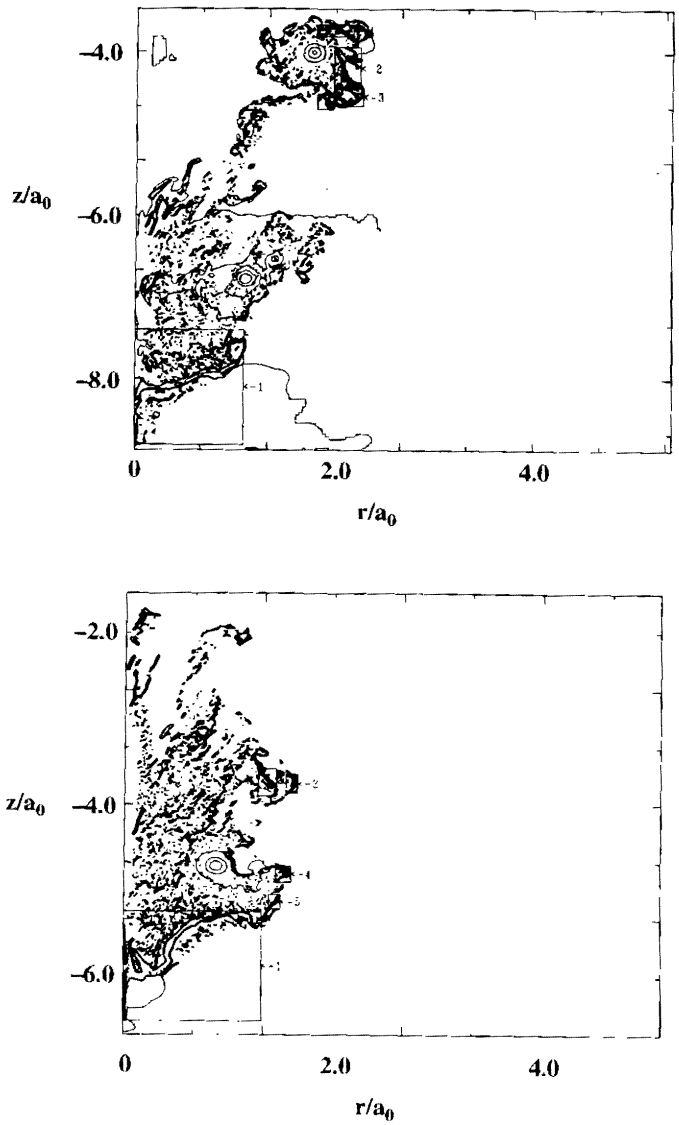

FIG. 19.—Comparison of a cloud in a wind ($\chi = 10$: *lower panel*) with a shocked cloud (standard case: *upper panel*) at $t = 6.32t_{cc}$. The initial Mach number of the cloud relative to the intercloud medium in the cloud-wind case is $M = 0.9$; in terms of the velocity v_b of a hypothetical shock that would lead to the same initial conditions, the initial conditions correspond to $v'_{c0} = -0.505v_b$ and $C_i = 0.56v_b$. The numbered boxes locate the largest fragments in order of mass in each case.

that in the shock-cloud case. The cloud undergoes a lateral expansion due to the Venturi effect. The axial stretching associated with material torn off the sides of the cloud is even greater, however, so that when the lateral expansion stops at t_m, the aspect ratio of the cloud is 1.4, as compared with 0.8 in the shock-cloud case. Our results are in agreement with those of Murray et al. (1993), who have studied this problem at lower resolution (R_{25}).

The circulation generated by the flow of the wind past the cloud is dominated by the postshock contribution given in equation (7.12a), $\Gamma_{post} = -1.5\,|\,v'_{c0}\,|\,a_0$, based on the measured drag time $3.79t_{cc}$. The measured circulation at time t_m is $-3.0\,|\,v'_{c0}\,|\,a_0$, about twice as large. Much of the discrepancy can be attributed to the initial conditions: at $t = 0$, the cloud was given a velocity v'_{c0}, so that the front face began with a finite circulation, whereas the back face acquired a circulation only after the flow had been established there. The contribution of the supersonic vortex ring is found to be small, $\sim +0.18\,|\,v'_{c0}\,|\,a_0$. The reduced level of the vorticity in the wind-cloud interaction as compared with the shock-cloud interaction is directly correlated with the longer destruction time in the wind-cloud case.

When a wind propagates through a cloudy medium, it entrains cloud material, and this can have a significant effect on both the thermal and dynamical properties of the wind. Hartquist et al. (1986) have developed a general approach to flows with entrained material, which they refer to as mass-loaded flows. They estimate that the rate at which mass is entrained by a wind flowing past a cloud at velocity v_w is

$$\dot{m}_c \propto M^{4/3}(m_c\, C_c)^{2/3}(\rho_i\, v_w)^{1/3}\,, \tag{9.3}$$

provided that the Mach number of the flow $M = v_w/C_i \lesssim 1$. Since we have not done a parameter study for the cloud-wind problem, we cannot verify their proposed scaling for the mass-loss rate, but we can verify their claim that the numerical coefficient in this relation is of order unity for the case we have considered. If we identify the cloud sound speed C_c as the initial sound speed, neglecting the small increases due to the weak shocks that propagate through the cloud as it interacts with the wind, then we have $C_c/C_i = \chi^{-1/2} = 0.316$. Furthermore, as remarked above, the Mach number for the case we have considered is $M = 0.9$. Estimating the entrainment time as $m_c/\dot{m}_{dest}$, where $t_{dest} = 6.15t_{cc}$ (Table 5), we find that the coefficient in the above expression is about 0.5 in this case. Our results are thus consistent with their estimate for the mass entrainment rate.

10. APPLICATION TO A SHOCKED CLOUD IN THE CYGNUS LOOP

Recently, new Hα images of the Cygnus Loop in the eastern region obtained by Fesen et al. (1992) have provided direct evidence for the interaction of a blast wave from a supernova remnant with an isolated interstellar cloud. Fesen et al. (1992) suggested that their data could be understood in terms of a shock-cloud interaction based on our preliminary results (Klein et al. 1990). Here we shall make a somewhat more detailed comparison of their observations with a calculation of a "radiative" cloud shock, where we have modeled the radiative losses in a cloud by using a ratio of specific heats in the cloud of $\gamma_c = 1.1$.

We can directly compare the observations of Fesen et al. (1992), which are reproduced in Figure 20 (Plate 1), with a

two-dimensional time snapshot of isocontours of density (Fig. 21). The direction toward the center of the Cygnus Loop is indicated on the observed Hα image in order to facilitate comparison with the calculation. Two separate timescales are involved: the intercloud crossing time $t_{ic} = 2a_0/v_b$, which is independent of density, and the cloud crushing time $t_{cc} = \chi^{1/2}a_0/v_b$, which increases with the density contrast. The relative position of the intercloud shock and the cloud at early times is determined by t_{ic}, whereas the dynamics of the shocked cloud is determined by t_{cc}. Following Fesen et al. (1992), we adopt an initial cloud radius $a_0 \simeq 0.5$ pc and a blast wave velocity $v_b \simeq 400$ km s^{-1}. As these authors point out, the estimate of a_0 is quite uncertain: it is based on assuming that a_0 is about equal to the thickness of the cloud, since the cloud appears to be flattened by about a factor of 2. With these numbers, the observed value of the intercloud crossing time is t_{ic}(obs) = 2440 yr. If we neglect the motion of the cloud (which is valid for large χ), then the separation between the cloud and the shock indicates that the interaction began 4100 yr ago (Fesen et al. 1992), so that at present t/t_{ic}(obs) = 1.68. Figure 21 shows the results of our calculation at $t/t_{ic} = 2.0$, close to the value inferred from observation. [Allowing for the motion of the cloud, which is about 0.25 pc for $\chi = 10$ from eq. (8.5) and Fig. 21, the observed age is increased to about 4700 yr, or $1.9t_{ic}$(obs).] Our calculations show that the intercloud shock interacts at a kinked angle behind the cloud and reattaches through a Mach disk. The observations show that the shock front indeed has very similar curvature so that predicted by the calculations. Furthermore, the observations show evidence of kinking and reattachment at the same relative locations as in the calculations, with some evidence of the appearance of the Mach disk. On the other hand, the observations show that the southern branch of the shock is more complex than either the northern branch or our calculations, suggesting that the ambient medium is denser there.

The evolution of the shocked cloud depends on the density ratio χ and is most easily followed in terms of the cloud crushing time t_{cc}. For example, the comparison of the observed and theoretical values of t/t_{ic} would proceed as above whether $\chi = 10$ or $\chi = 100$, but at $t/t_{ic} \sim 2$ the cloud is far more distorted in the former case than in the latter. Fesen et al. (1992) suggest that the appropriate value of χ for the cloud in the Cygnus Loop is about 10, and the similarity in the morphology of the observed shocked cloud to our calculations shows that this is a good estimate. For this value of χ, the cloud crushing time is $t_{cc} = 3900$ yr; the snapshot in Figure 21 is at a time $1.26t_{cc}$. Our calculations predict that after the shock has swept over the cloud, it produces a strong shear surface along the cloud boundary. The resulting Kelvin-Helmholtz instabilities and vortex rings stretch, fragment, and distort the cloud, producing armlike features that are swept back downstream. The convergence of the intercloud shock on the back side of the cloud drives a shock into the rear of the cloud that interacts with the transmitted shock within the cloud, resulting in a highly flattened cloud core attached to the distorted, backswept arms. This cloud morphology is clearly seen in our calculations and can also be seen in the Hα observations. Our calculations enable us to predict the velocity dispersion for the cloud, which we find to be $\delta v_z \simeq 60$ km s^{-1} in the axial direction and $\delta v_r \simeq 40$ km s^{-1} in the radial direction. If the cloud is indeed spherical (which it may not be; see below), then the position of the cloud near the edge of the blast wave as projected on the plane of the sky implies that δv_r is the relevant velocity dispersion for our line of sight.

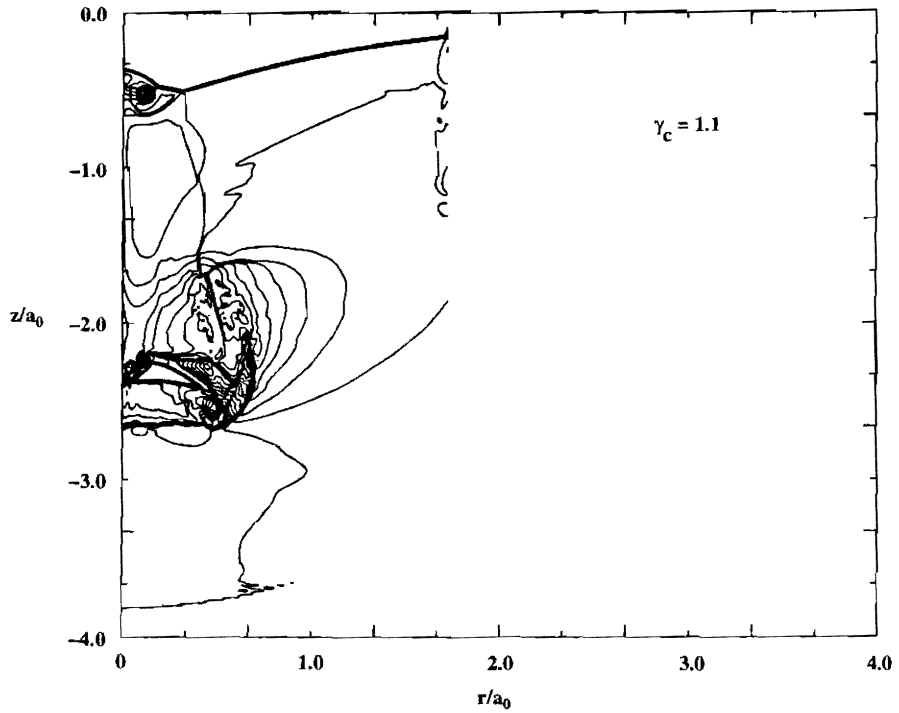

FIG. 21.—Shocked cloud in the Cygnus Loop: density contorus for a shocked cloud at $t = 1.26t_{cc} = 1.99t_{ic}$ with a density contrast $\chi = 10$ and a soft equation of state ($\gamma_c = 1.1$), similar to the conditions inferred for the shocked cloud in the Cygnus Loop observed by Fesen et al. (1992). The contour at $z \simeq -4.0a_0$ indicates the presence of the reflected bow wave. As in Fig. 16, the density contours extend only to $r = 1.67a_0$.

Fesen et al. (1992) have suggested that the emission feature they find on the western side of the observed cloud is the reflected shock from the interaction of the blast wave as it first encountered the cloud. However, we believe that the feature Fesen et al. (1992) have identified is not the bow shock (which they term the "reverse shock") but rather an unrelated feature seen in projection. For $\chi \simeq 10$, the bow shock soon settles into a bow wave rather than a shock. The bow shock must be concave with respect to the cloud, not convex as indicated in the observations. Finally, the feature that Fesen et al. (1992) identify as the bow shock is far too bright, with emission comparable to the blast wave emission. The emission at the blast wave shock is due to ionization of hydrogen; once the intercloud gas is ionized, it should no longer be visible optically.

Recent X-ray observations of the eastern cloud (J. R. Graham 1993, private communication) have revealed that the X-ray emission from the shocked intercloud gas is restricted to the region behind the sharp Hα feature demarking the shock front (see Fig. 20). Graham has pointed out that this observation has important implications for the initial morphology of the cloud. For a spherical cloud, such as we have considered, the emission should be axially symmetric. The emission along a line of sight just in front of the section of the intercloud shock that we have identified as the Mach disk should thus be the same as that along a similar line of sight in the plane of the sky. As shown in Figure 20, such a line of sight passes through the shocked intercloud gas, which Graham's observations show to be emitting X-rays. The observations thus appear to be inconsistent with a cloud that is roughly spherical: there is little or no X-ray emission along our line of sight just in front of the Mach disk, whereas the observations show that there would be X-ray emission along a similar line of sight in the plane of the sky. We interpret these observations as indicating that the cloud is elongated along the line of sight—the cloud is cylindrical rather than spherical. A cylindrical cloud will cause an indentation in the shock along its entire length, sharply cutting off the X-ray emission in a manner consistent with the observations. This interpretation is consistent with that of other optical emission in the Cygnus Loop, which generally requires observed features to be elongated along the line of sight (e.g., Hester & Cox 1986). Although we have not calculated the interaction of a shock with a cylindrical cloud, we expect that the overall dynamics is similar to that for a spherical cloud; this is consistent with the results of Mac Low et al. (1994) for the MHD case. However, a three-dimensional calculation would be needed to predict the expected value of the velocity dispersion in this case.

11. CONCLUSIONS

We have made a detailed numerical investigation of the interaction of a shock wave propagating through an intercloud medium with an embedded cloud, using for the first time a second-order–accurate Godunov method with local adaptive mesh refinement to achieve heretofore unobtainable numerical resolution. We have assumed that radiative losses are negligible, which in practice restricts direct application of our results to fast shocks (eq. [2.12]). However, we have studied the qualitative effects of radiative losses by considering a cloud with a specific heat ratio $\gamma_c = 1.1$ (the specific heat ratio of the intercloud gas is always assumed to be $\gamma_i = 5/3$). For simplicity, we have assumed that the pressure behind the shock propagating in the intercloud medium is constant, which in practice limits our considerations to small clouds (§ 2.2). With these restrictions, the shock-cloud interaction depends on only three dimensionless parameters, the cloud-intercloud density ratio $\chi \equiv \rho_{c0}/\rho_{i0}$, the Mach number of the shock, M, and the specific heat ratio of the cloud, γ_c. Pressure balance ensures that the cloud shock velocity v_s and the intercloud shock velocity v_b are related by $\rho_{c0} v_s^2 \simeq \rho_{i0} v_b^2$. As a result, the characteristic dynamical time a_0/v_s is about equal to the cloud crushing time, $t_{cc} \equiv \chi^{1/2} a_0/v_b$.

Our basic result is that the cloud is decelerated and destroyed in several cloud crushing times. This result is independent of the parameters of the problem, at least over the range we have considered; indeed, it does not depend on the assumption of a spherical cloud or even on the presence of an initial blast wave. Previous authors (e.g., Nittman et al. 1982; Bedogni & Woodward 1990) have come to a similar conclusion on the destructiveness of the shock-cloud interaction on the basis of more limited studies. This timescale is considerably shorter than the naive estimate that the cloud must sweep up a column density of material comparable to its initial value. The high pressure in the cloud produced by shocks combined with the low pressure on the sides of the cloud due to the flow of intercloud gas result in a lateral expansion of the cloud that hastens its deceleration and destruction. The cloud is destroyed by the combined action of the Kelvin-Helmholtz and Rayleigh-Taylor instabilities.

The rate of deceleration is characterized by the drag time t_{drag}, which is the time for the relative velocity of the cloud and the intercloud medium to decrease by a factor e. Similarly, the rate of fragmentation is characterized by the destruction time t_{dest}, which is the time for the mass of the largest cloud fragment to become less than the cloud mass by a factor e. As χ increases from 3 to 100, t_{drag} increases from $1.6t_{cc}$ to $3.4t_{cc}$; over the range 10–400, t_{dest} drops $4t_{cc}$ to about $2.0t_{cc}$. These results are independent of the Mach number of the shock, so long as it is large. In many cases $t_{drag} \lesssim t_{dest}$, so that effective acceleration can occur; this is in contrast to the claims of Nittman et al. (1982). After fragmentation, the cloud material continues to be accelerated until it is approximately comoving with the intercloud gas. A simple theory for the acceleration of the cloud was developed in § 6 which accounts for most of our results on cloud drag to within a factor of about 1.5.

Substantial amounts of vorticity are generated in the shock-cloud interaction, and we have developed a model that can account for this vorticity quantitatively. Three major sources of vorticity were identified: the action of the initial shock passing over the cloud, the subsequent flow past the cloud, and the generation of a supersonic vortex ring when a Mach reflected shock forms behind the cloud. Much of the vorticity is concentrated at the boundary between the cloud and the intercloud medium. As a result of the Kelvin-Helmholtz instability, this shear layer is severely distorted, producing vortex rings with embedded cloud fragments. Vortical motions in the cloud material produce an observable velocity dispersion in the radial direction (perpendicular to the axis of symmetry) amounting to about $0.1v_b$.

The fragmentation of the cloud can be characterized by two timescales: the destruction time, t_{dest}, which is the time at which the mass of the cloud core has been reduced from the initial cloud maps by a factor e, and the mixing time, t_{mix}, which is the time at which half the mass of the cloud has been shredded so finely that it is in zones that contain both cloud and intercloud material. The destruction time is about $3.5t_{cc}$ for density ratios in the range 10–100; during this time the

blast wave will advance a distance $3.5\chi^{1/2}a_0$. For the range of χ we have considered, the mixing time is at least as large as the destruction time. The mixing appears to be due to the Kelvin-Helmholtz instability, and a simple model has been developed (§ 8) which is in good agreement with the χ-scaling observed in the numerical experiments. We find that clouds with χ in the range 10–100 can be displaced no more than about 8 cloud radii before they have become mixed with the intercloud medium.

The principal limitation of our simulations is that they are restricted to two dimensions. It is known that the vortex rings that are so prominent in the shock-cloud interaction are unstable (Widnall, Bliss, & Tsai 1974). Despite the presence of such instabilities, however, three-dimensional simulations demonstrate that the results presented here are by and large valid in three dimensions as well (Stone & Norman 1992; Klein et al. 1994b).

A possible example of a shocked cloud has recently been discovered by Fesen et al. (1992) in the Cygnus Loop. Comparison of our results for the "radiative" ($\gamma_e = 1.1$) model with their observations indicates that our overall predictions of a highly flattened cloud core attached to swept-back, fragmented arms are in good agreement with the observed cloud morphology. The structure of the intercloud shock and its separation from the cloud are in good agreement with the observations for a density ratio $\chi = 10$. X-ray observations by J. R. Graham (1993, private communication) are not consistent with a spherical cloud, but rather suggest that the cloud is elongated along the line of sight. Supernova remnants such as the Cygnus Loop provide cosmic laboratories in which to study the interaction of shock waves with gas clouds, and future observations and numerical experiments should further elucidate the physics of this interaction.

We thank M. Mac Low for a number of valuable conversations, and J. Ostriker for emphasizing the importance of vorticity in the cloud-shock problem. We are grateful to J. Scalo for providing valuable insight into the production of vorticity in curved shocks. We also thank J. R. Graham for giving permission to discuss his X-ray results in advance of publication, and R. Fesen for permission to reproduce his data on the Cygnus Loop (Fig. 20). T. Kelleher provided valuable help in constructing global quantities from data in nested grids. The research of C. F. M. is supported in part by grants from the National Science Foundation, AST 89-18573 and AST 92-2189. Both R. I. K. and C. F. M. have benefited from the support of a NASA grant to the Center for Star Formation Studies. The computations were carried out on the YMP 8/128 supercomputer at LLNL. P. C. is supported by the Army Research Office under grant DAAL03-88-K-0197, by DARPA and the NSF under grants DMS-8919074 and PYI Award ACS-8958522, and at LLNL by the Applied Mathematical Sciences Program. This work was performed in part under the auspices of the US Department of Energy at the Lawrence Livermore National Laboratory under contract W-7405-ENG-48.

REFERENCES

Balbus, S. A. 1986, ApJ, 304, 787
Balbus, S. A., & McKee, C. F. 1982, ApJ, 252, 529
Bedogni, R., & Woodward, P. R. 1990, A&A, 231, 481
Berger, M. J., & Colella, P. 1989, J. Comput. Phys., 82, 64
Berger, M. J., & Oliger, J. 1984, J. Comput. Phys., 53, 484
Bonnor, W. B. 1956, MNRAS, 116, 351
Braun, R., & Strom, R. G. 1986, A&A, 164, 208
Bychkov, K. V., & Pikel'ner, S. B. 1975, Soviet Astron. Lett., 1, 14
Castor, J., McCray, R., & Weaver, R. 1975, ApJ, 200, L107
Chandrasekhar, S. 1961, Hydrodynamic and Hydromagnetic Stability (New York: Dover)
Colella, P., & Woodward, P. R. 1984, J. Comput. Phys., 54, 174
Cowie, L. L., & McKee, C. F. 1977, ApJ, 211, 135
Cowie, L. L., McKee, C. F., & Ostriker, J. P. 1981, ApJ, 247, 908
Cox, D. P., & Smith, B. W. 1974, ApJ, 189, L105
Draine, B. T., & Giuliani, J. L. 1984, ApJ, 281, 690
Ebert, R. 1955, Z. Astrophys., 37, 222
Falle, S. A. E. G. 1989, in Structure and Dynamics of the Interstellar Medium, ed. G. Tenorio-Tagle, M. Molez, & J. Melnick (New York: Springer-Verlag), 152
Fesen, R. A., Kwitter, K. B., & Downes, R. A. 1992, AJ, 104, 719
Glaz, H. M., Colella, P., Glass, I. I., & Deschambault, R. L. 1985, Proc. R. Soc. Lond., A, 398, 117
Hartquist, T. W., Dyson, J. E., Pettini, M., & Smith, L. J. 1986, MNRAS, 221, 715
Heathcote, S. R., & Brand, P. W. J. L. 1983, MNRAS, 203, 67
Hester, J. J., & Cox, D. P. 1986, ApJ, 300, 675
Hornung, H. 1986, Ann. Rev. Fluid Mech., 18, 33
Klein, R. I., Colella, P., & McKee, C. F. 1992, in Advances in Compressible Turbulent Mixing, ed. W. Dannevik, A. Buckingham, & C. E. Leith (Washington, DC: GPO), 452
———. 1994a, in preparation (Paper II)
Klein, R. I., McKee, C. F., & Bell, J. 1994b, in preparation
Klein, R. I., McKee, C. F., & Colella, P. 1990, in The Evolution of the Interstellar Medium, ed. L. Blitz (San Francisco: ASP), 117
Krebs, J., & Hillebrandt, W. 1983, A&A, 128, 41
Lada, C. J. 1985, ARA&A, 23, 267
Landau, L. D., & Lifshitz, E. M. 1959, Fluid Mechanics (Reading: Addison-Wesley)
Mac Low, M.-M., McKee, C. F., Klein, R. I., Stone, J., & Norman, M. 1994, in preparation
McKee, C. F. 1988, in IAU Colloq. 101, Supernova Remnants and the Interstellar Medium, ed. R. S. Roger & T. L. Landecker (Cambridge: Cambridge Univ. Press), 205
———. 1990, in The Evolution of the Interstellar Medium, ed. L. Blitz (San Francisco: ASP), 3
McKee, C. F., & Cowie, L. L. 1975, ApJ, 195, 715
McKee, C. F., Cowie, L. L., & Ostriker, J. P. 1978, ApJ, 219, L23
McKee, C. F., Hollenbach, D. J., Seab, C. G., & Tielens, A. 1987, ApJ, 318, 674
McKee, C. F., & Ostriker, J. P. 1977, ApJ, 218, 148
Murray, S. D., White, S. D. M., Blondin, J. M., & Lin, D. N. C. 1993, ApJ, 407, 588
Nittman, J., Falle, S., & Gaskell, P. 1982, MNRAS, 201, 833
Nulsen, P. E. J. 1982, MNRAS, 198, 1007
Odenwald, S. F., & Shivanandan, K. 1985, ApJ, 292, 460
Öpik, E. G. 1953, Irish Astron. J., 2, 219
Oettl, R., Hillebrandt, W., & Müller, E. 1985, A&A, 151, 33
Ostriker, J. P., & McKee, C. F. 1988, Rev. Mod. Phys., 60, 1
Picone, J. M., & Boris, J. P. 1988, J. Fluid Mech., 1989, 23
Raymond, J. C., Cox, D., & Smith, B. W. 1976, ApJ, 204, 290
Richtmyer, R. D. 1960, Comm. Pure Appl. Math., 13, 297
Rozyczka, M., & Tenorio-Tagle, G. 1987, A&A, 176, 329
Schwartz, R. D. 1983, ARA&A, 21, 209
Sgro, A. G. 1975, ApJ, 197, 621
Spitzer, L. 1982, ApJ, 262, 315
———. 1990, ARA&A, 28, 71
Stone, J. M., & Norman, M. L. 1992, ApJ, 390, L17
Tenorio-Tagle, G., & Rozyczka, M. 1986, A&A, 155, 120
van den Bergh, S. 1971, ApJ, 165, 457
White, R. L., & Long, K. S. 1991, ApJ, 373, 543
Widnall, S. E., Bliss, D. B., & Tsai, C. Y. 1974, J. Fluid Mech., 66 (Part 1), 35
Woodward, P. R. 1976, ApJ, 207, 484
Yang, X., Chern, I.-L., Zabuskey, N. J., Samtaney, R., & Hawley, J. F. 1992, Phys. Fluids A, 4, 1531

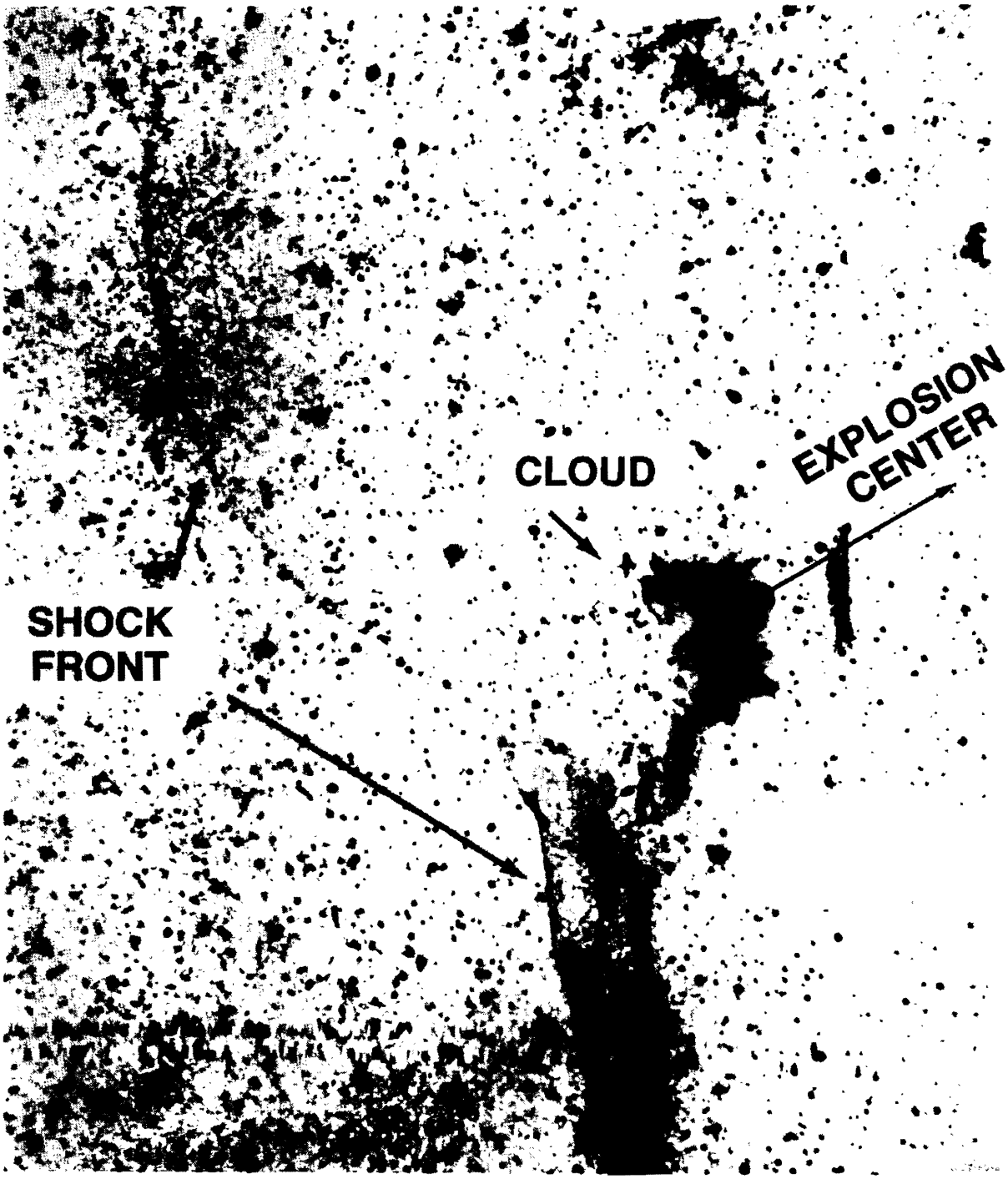

FIG. 20.—Hα image of an isolated emission cloud along the eastern limb of the Cygnus Loop, reproduced with permission from Fesen et al. (1992). The arrow indicates the approximate direction of the center of the Cygnus Loop. The label suggesting the location of the bow shock has been removed from the original for the reasons given in the text.